UNIVERSIDAD DE CONCEPCIÓN
FACULTAD DE CIENCIAS FÍSICAS Y MATEMÁTICAS
DEPARTAMENTO DE FÍSICA

TESIS DE MAGÍSTER

FIRST-ORDER PHASE TRANSITION AND CLUSTER DYNAMICS IN THE Q2R-POTTS CELLULAR AUTOMATON

POR

JIM TORTELLA GANA

Profesor guía: Dr. Felipe Urbina
Profesor co-guía: Dr. Félix Borotto

27 de marzo de 2024.
Concepción, Chile.

DOCUMENTO PRESENTADO A LA FACULTAD DE CIENCIAS FÍSICAS Y MATEMÁTICAS DE LA UNIVERSIDAD DE CONCEPCIÓN EN CUMPLIMIENTO PARCIAL DE LOS REQUERIMIENTOS PARA EL GRADO DE MAGÍSTER EN CIENCIAS CON MENCIÓN EN FÍSICA.

Dedicado a mis padres:
Nicole Alejandra Gana Gómez y José Hernán Tortella Urrea.

AGRADECIMIENTOS

Agradezco a todas las personas quienes me han entregado su amor, tiempo, o ambos, en las muchas formas posibles. Recursos irreversibles.

Contents

List of Tables

List of Figures

Resumen

Los autómatas celulares (AC) son sistemas dinámicos discretos que permiten el estudio de fenómenos emergentes desde una perspectiva microscópica, o *bottom-up*. En esta tesis, nos centramos en el modelo Q2R-Potts, un autómata celular específico que es reversible y conservativo tanto en el sentido matemático como físico. Este modelo se distingue por un espacio de fases compuesto de puntos fijos y ciclos límite, y una cantidad conservativa similar a la energía. Adaptamos la formulación original del modelo, que se desarrolló en dos dimensiones con $q = 3$ estados, a una cadena unidimensional, con el objetivo de caracterizar su dinámica tanto a nivel macroscópico como microscópico.

Inicialmente, realizamos una caracterización completa del espacio de fases para una cadena de longitud $L = 6$, analizando la energía de cada configuración, su período y la dinámica de clusters acumulados. Este análisis inicial fue esencial para comprender la distribución de la complejidad en el autómata, especialmente en términos de la riqueza de periodos y configuraciones para una energía dada. Posteriormente, extendimos nuestro estudio a cadenas de longitudes $L = 256$, $L = 512$ y $L = 1024$, construyendo diagramas de fase de magnetización versus densidad de energía. Aquí, descubrimos una transición de fase de primer orden en una región crítica de energía, que converge a $-0.9 > E/L > -0.88$ a medida que aumentamos la longitud del sistema. Se establece $L = 1024$ como la longitud característica del sistema y utilizamos esta dimensión para explorar más a fondo la dinámica microscópica introduciendo el concepto de cluster de estados. Estos últimos, muestran un comportamiento de ley de potencias y auto-organización que depende de la energía de la configuración.

Este estudio aporta una nueva perspectiva a la comprensión de las transiciones de fase en el modelo Q2R-Potts, estudiando por primera vez una transición de fase de primer orden en los modelos Q2R, enfatizando su relevancia física y su comportamiento no ergódico. Nuestros hallazgos abren caminos para futuras investigaciones en sistemas discretos con comportamientos emergentes complejos, particularmente en extensiones del modelo Q2R-Potts a dos y tres dimensiones.

Abstract

Cellular automata (CA) are discrete dynamical systems that allow the study of emergent phenomena from a bottom-up point of view. In this thesis, we focus on the Q2R-Potts model, a specific cellular automaton that is reversible and conservative both mathematically and physically. This model is distinguished by a phase space composed of fixed points and limit cycles, and possesses a conservative quantity akin to energy. We adapted the original formulation of the model, developed in two dimensions with $q = 3$ states, to a one-dimensional chain aiming to characterize its dynamics both macroscopically and microscopically.

Initially, we conducted a comprehensive characterization of the phase space for a chain of length $L = 6$, analyzing the energy of each configuration, its period, and the microdynamics by measuring the accumulated state clusters. This initial analysis was crucial for understanding the complexity distribution in the automaton, particularly in terms of the richness of periods and configurations for a given energy. Subsequently, we extended our study to chains of lengths $L = 256$, $L = 512$ and $L = 1024$ constructing phase diagrams of magnetization versus energy density. We discovered a first-order phase transition in a critical energy region that converges to $-0.9 > E/L > -0.88$ while increasing the chain's size. Then, we determined $L = 1024$ as the characteristic length and used this chain size to further explore the microdynamics of the system, introducing the concept of state clusters. The aforementioned exhibits a power-law behavior and self-organization depending on the energy governing the system configuration.

Finally, this study offers a new perspective on understanding phase transitions in the Q2R-Potts model, approaching for the first time in the family of Q2R a first-order phase transition, emphasizing its physical relevance and non-ergodic behavior. Our findings pave the way for future research in discrete systems with complex emergent behaviors, particularly in extensions of the Q2R-Potts model to two and three dimensions.

Chapter 1

Introduction

Models exhibiting highly complex behavior are often studied using the tools of statistical physics, particularly when their dynamics involve interactions. Examples of such systems include active particle models [1, 2], particle transport models [3, 4], spin models [5, 6], and cellular automata (CA) models [7, 8]. Those research are typically investigated through extensive numerical simulations, where their dynamics are analyzed using well-defined parameters. These parameters can represent either conservative or non-conservative quantities that evolve over time.

In recent decades, several approaches have been published to explore and understand the dynamics of these systems, keeping a focus on cluster formation, i.e., particles having a specific feature in common. In this context, Soto and Golestanian [9] studied a run-and-tumble bacterial model by presenting a theoretical framework for finding the cluster size distribution in a one-dimensional system. Conversely, Cardy and Ziff [10] presented and verified the size distribution of clusters ($N(l) \sim C/l^2$) by getting exact results about the proportionality constant C associated with the macroscopic measure of the large clusters for the Percolation, Ising, and Potts Models. Also, Kohyama [11], investigating the properties a family of cellular automata, found a gas-liquid phase and liquid droplets by using the idea of cluster growth.
Given the advancements mentioned above, it becomes evident that quantifying clusters and their dynamics can reveal significant aspects of various systems. An intriguing model for such exploration is the Q2R model, as defined by Vichniac [7]. This model represents a second-order cellular automaton characterized by reversible dynamics and a conservative energy-like function [12]. Its features make it particularly suitable for studying particle interactions and cluster behavior, providing insights into the complex mechanisms underlying these phenomena.
This model has its roots in the Ising model for describing ferromagnetic transitions. In fact, in two dimensions, the Q2R cellular automaton shows a phase transition around a critical energy density value [13, 14] that is very close to that found in the Ising model $E_c \approx -\sqrt{2}$. On the other hand, Urbina and Rica [15] characterized equilibrium and non-equilibrium statistical properties using a coarse-graining technique, and this allowed for the writing of a probability transfer matrix to define a master equation. Due to the reversibility of this model, Herrmann et al. [13] demonstrated that the model dynamics can have periods of “infinite" length on lattices of “infinite" size. In this context, Montalva et al. [16] classified the entire space of $2^{32} \approx 4.3 \times 10^9$ configurations by identifying all the fixed points and the orbits for each energy's value. Moreover, they presented a theorem that classifies the different types of cycles: symmetric and asymmetric. Then, Urbina [17] presented a three-dimensional extension of the model and introduced a coupling constant which evolves into three kinds of phases.

The above discussion demonstrates that the Q2R model has been extensively studied in various aspects, but it has always been considered as a binary system. However, an extension of the Q2R cellular automaton to the two-dimensional Potts model, considering q states, was defined by Pomeau and Vichniac [47]. This extension preserves the reversible dynamics and conservative quantities of the original model. This CA emerges as a promising framework for studying dynamics where the Potts model plays a role, employing a set of simple logical rules. Potential studies under this framework might include other phenomena such as recrystallization [18], cellular growth [19], and percolation [20]. In this work, we will study the dynamics of the Q2R-Potts model using a one-dimensional chain. Here, we will employ tools of statistical physics to quantify global behaviors using phase diagrams and probability distribution functions. To characterize the cellular automaton, we will use the cluster concept for different energy

density values to quantify microscopic order and disorder.

This thesis starts with research questions and methodology, followed by a foundational exploration of cellular automata, elementary statistical mechanics useful for our purposes and an overview of lattice models and the genesis of the Q2R model in Chapters 2, 3 and 4 respectively. After that, in chapter 5 is detailed the original Q2R-Potts model formulation and in Chapter 6 is described the initial conditions and parameters for our adaptation to the one-dimensional case. Our findings are in Section 6.4. Concluding Chapter 7 synthesize these insights, reflecting on their implications and future avenues for research in this fascinating intersection of computational physics and lattice models. Finally, in appendix A are additional figures with the behavior of this model for different sizes studied.

Goals and Research Questions

The main goal of this thesis is to characterize the Q2R cellular automaton (CA) in its extension to the Potts model with $q = 3$ states in the one-dimensional case using tools from statistical mechanics. The questions guiding our research are the following:

1. How is composed the Q2R-Potts CA's phase space?
2. Does the Q2R-Potts CA undergo a phase transition, and if so, what type of transition is it?
3. How does the microscopic dynamic evolve in the system?
4. Can the microscopic dynamics capture and reflect the physical properties of the system?

To address these questions, we will conduct a series of simulations. Initially, we will explore the phase space of the Q2R-Potts CA by classifying all configurations for a chain of length $L = 6$ in terms of their energy, period, and accumulated clusters. This analysis will provide insights into both the macroscopic and microscopic dynamics of the system from larger sizes.

Subsequently, we will investigate chains of sizes $L = 256$, $L = 512$ and $L = 1024$ to examine their macroscopic properties. By constructing phase diagrams of magnetization versus energy density, we aim to identify any potential phase transitions and determine a characteristic length scale L_c that accurately represents the system's behavior. Following this, we will focus on the chain of size L_c to delve deeper into its microscopic dynamics, exploring how these small-scale interactions influence the overall behavior of the model.

This comprehensive approach will enable us to gain a deeper understanding of the Q2R-Potts model and its applications in statistical physics, contributing to the broader field of complex systems analysis.

Chapter 2

Cellular Automata

Cellular automata are discrete dynamical systems in space and time [21]. Although they could be defined in any dimension and adopt different geometries, one of the most used and simple ways to represent them is through a bidimensional lattice of homogeneous cells. Each cell adopts one of the possible states available in the system, where this value will evolve following a rule of local interactions but is applied globally. This means that over each cell, the same rule is applied, taking into account the local interactions of each one. Thus, we can think of the rule of evolution as a function whose arguments are the state to evolve, its neighbors, and time.

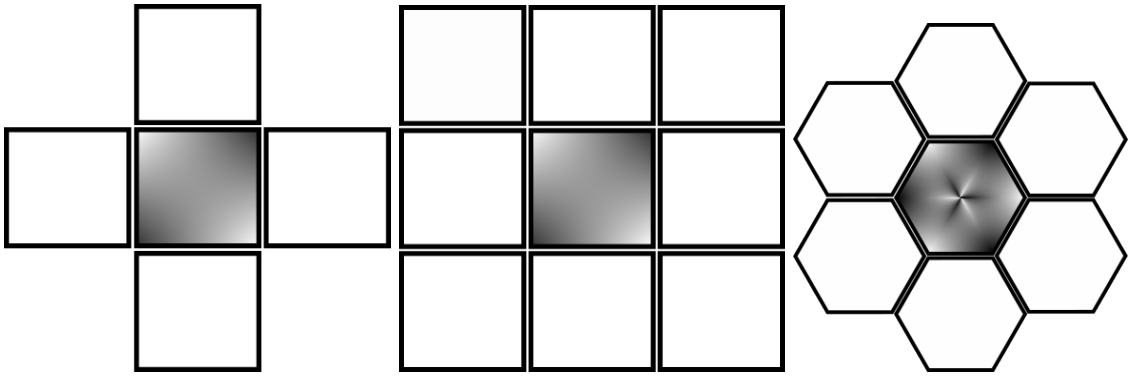

(a) (b) (c)

Figure 2.1: Two-dimensional cellular automata with square and hexagonal geometry, considering different neighbors for the blackened cell. In (a) we can see the von Neumann neighborhood, in (b) the Moore neighborhood is represented, and in (c) we can observe the first neighbors of a cell in a hexagonal lattice. Source: Own Elaboration

This rule of evolution could yield different patterns, but the most striking is related to the nature of these rules because they can be defined following logical algorithms from which it is not straightforward to predict the general behavior of the system after a certain number of steps (see Figure 2.2).
The development of cellular automata is intimately related to computing, thanks to the significant contributions of John von Neumann in this field [22], and his curiosity about the numerical analysis that computers could offer. Thus, their conception dates back to 1948 when von Neumann, curious about the biological nature of self-replication, proposed the *kinematic model* [23], whose formalism includes a continuous space. While discussing the technical difficulties of formalizing this idea with Stanislaw Ulam, Ulam suggested discretizing the space for simplicity's sake. This collaboration led to the creation of von Neumann's self-replicating cellular automaton. Where the space was represented using a square lattice and each cell could assume one of the 29 possible states [23].
In addition to the kinematic model and cellular automata, von Neumann devised the following models:

- **The excitation-threshold-fatigue model:** It possesses the same characteristics as the self-replicating automaton, but its rule of evolution incorporates excitation and fatigue thresholds,

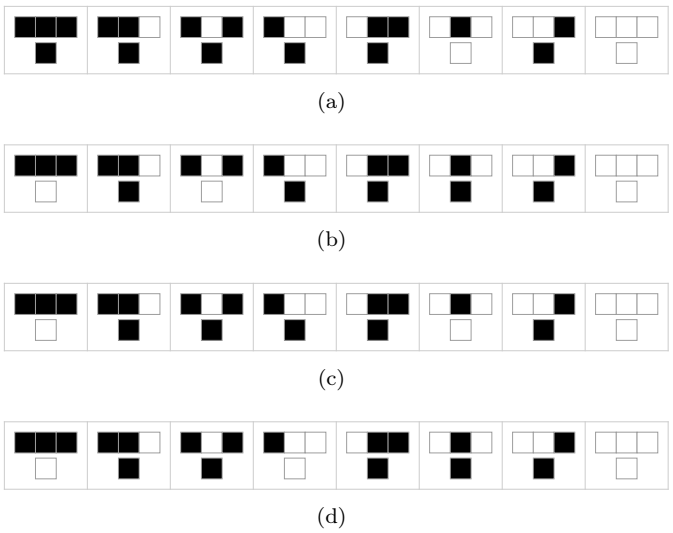

Figure 2.2: Representation of different rules for one-dimensional cellular automata. The top row in each box represents the state to evolve (central cell) and its two first neighbors; the bottom row represents the evolution of the central state based on its two neighbors. In each picture, based on the Wolfram nomenclature, we have the rules: (a) 250, (b) 94, (c) 122, and (d) 110, respectively. Source: Own Elaboration

aiming to simulate neuronal behavior.

- **The continuous model:** Here, von Neumann planned to use cellular automata in a heuristic way to understand and solve nonlinear partial differential equations associated with diffusive processes in fluids.
- **Probabilistic automata:** This model incorporates a probabilistic variable in the rule of evolution instead of a purely deterministic rule.

It's worth noting that while these models were conceptualized by John von Neumann, they were not fully developed due to his premature death. Despite this, the development of cellular automata remained tied to mathematics and computer science, serving as an important model for parallel processing and image recognition [24, 25]. Furthermore, they have been applied in various fields including physics, military strategy, social sciences, and more [26, 27, 28, 29].

Beyond the theoretical and applied developments that cellular automata have undergone over the years, one of the most significant advances in the subject is attributed to Stephen Wolfram's works [30]. This culminated in the publication of a book [31] aiming to profoundly change the way we conceive and study complexity in science.
The British physicist approached cellular automata as a study subject in its own right, focusing comprehensively on their properties, behaviors, and inherent features, unraveling their potential depth. For example, in his research, he categorized the pattern formation of cellular automata, starting from random initial conditions, into four types:

- **Class 1:** The evolution of the system leads to a uniform final state where all the cells have the same value (Figure 2.3(a)).
- **Class 2:** The evolution of the system leads to steady or periodic states with well-defined structures that do not interact between them (Figure 2.3(b)).
- **Class 3:** The evolution of the system results in the emergence of well-defined structures, such as triangles, which appear seemingly at random and without any periodicity (Figure 2.3(c)).
- **Class 4:** The evolution of the system leads to well-defined structures that interact between them in an irregular and unpredictable way (Figure 2.3(d)).

All automata, regardless of their geometry or dimension, exhibit the behaviors outlined by Wolfram. However, since this classification is qualitative, there are some *borderline* automata whose behavior cannot

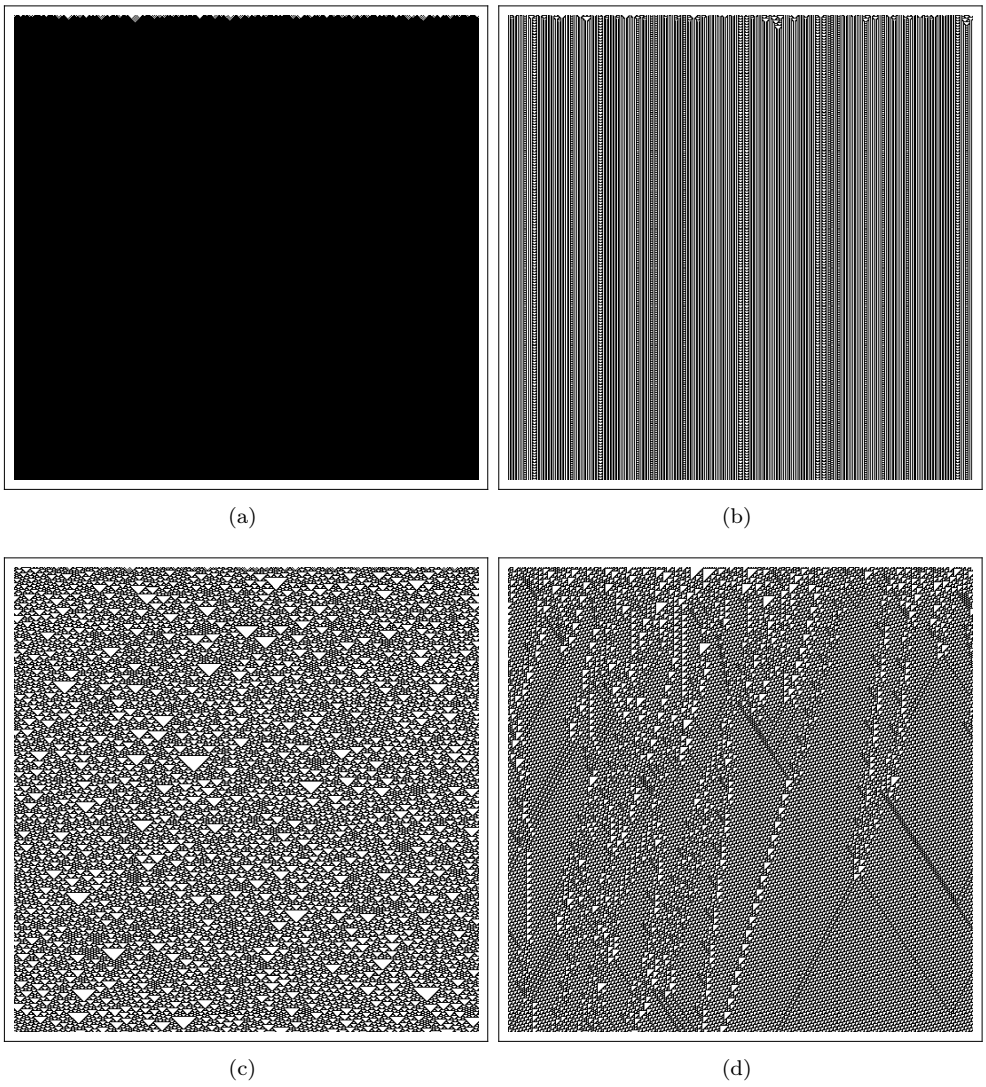

(a) (b)

(c) (d)

Figure 2.3: Examples of evolution over time of one-dimensional cellular automata considering four rules that lead to different classes defined by Wolfram. The black cells represent ones, and the white cells represent zeros. Each row represents the state of the cellular automaton at a given time and the evolution over time can be seen by scanning the rows downwards. In each figure, we have the rules: (a) 250, (b) 94, (c) 122, and (d) 110, respectively (see Figure 2.2). Source: Own Elaboration

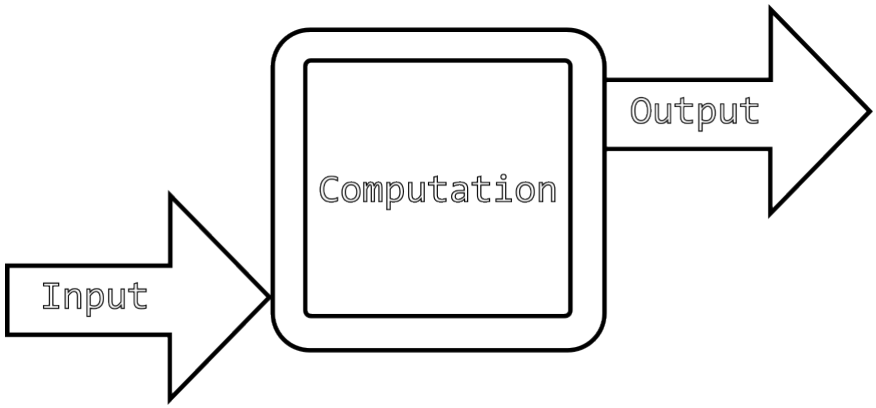

Figure 2.4: Schematic representation of the relationship among the three key processes in a computational system: input, computation, and output. Source: Own Elaboration

be unambiguously categorized, although such cases are rare according to Wolfram [31]. Additionally, certain evolutionary rules, such as rule 110, can mimic the behaviors of other rules. Such rules are termed "Universal." Given the appropriate initial conditions, they can simulate any algorithm executed by a Turing machine [32].
In simple terms, a Turing machine is a theoretical model that represents computations through logical procedures and operations of reading and writing on an infinite tape [33]. This model embodies the foundational concept behind computers and their computational capabilities. Thus, a universal cellular automaton can, in theory, compute anything using specific logical rules.
Wolfram's discoveries prompted him to delve deeper into his ideas regarding the workings of computational systems and their relationship with natural phenomena. In general, a computational system can be understood through three stages:

1. **Input:** Corresponds to the information provided to be processed by a system.
2. **Computation:** This stage consists of processing the input following a set of well-defined rules or instructions.
3. **Output:** Information that emerges from the system after acting over the input.

Given that universality is achieved by rule 110, Wolfram posits that all cellular automata with Class 4 behavior are also universal. This led him to suggest a computational threshold for all systems. Once this threshold is surpassed, a system becomes universally and computationally equivalent to any other system. This universality isn't contingent on the complexity of a system's underlying rules but rather on how the system processes information.
He went even further, suggesting that all phenomena in nature, regardless of their specific characteristics, can be perceived as computational processes. Although each phenomenon may operate under distinct rules, once they reach the universality threshold, they exhibit equivalent levels of sophistication, capable of processing information similarly. Wolfram coined this the **Principle of Computational Equivalence**.
This computational perspective led Wolfram to build upon Turing's concept of "computability" [33], introducing the notion of **Computational Irreducibility**. As Turing proposed, some processes are computable (resolved in a finite number of steps), and those that aren't. Computational Irreducibility expands on this, suggesting some processes are so complex that their outcomes cannot be shortcut or predicted in advance. The progression of such processes can only be understood by letting them unfold entirely. This idea is exemplified by the behaviors of different cellular automata classes: Classes 1 and 2 illustrate computationally reducible processes because their outcomes are predictable within a finite number of steps. In contrast, Classes 3 and 4 epitomize computationally irreducible processes, where the evolution of structures remains uncertain over time.

While bold, the idea of understanding nature as a computational process remains a topic of robust discussion and is far from being an openly accepted principle in the way we conduct science today. Nev-

ertheless, from their inception, cellular automata were designed as tools to gain intuition into phenomena that were difficult to understand by other means. In this sense, cellular automata have been a successful foundation for models such as the *run and tumble* [34], which can be viewed as a *probabilistic automaton* that models the behavior of certain bacteria, and also for agent-based models [35], widely used to simulate collective behaviors of various kinds. However, some models can be directly conceptualized as a cellular automaton, which we will review in Chapter 4.

Chapter 3

Some Elements of Statistical Mechanics and Phase Transitions

Among the objectives of this thesis is the characterization of a specific cellular automaton using the tools of statistical mechanics. Therefore, in this chapter, I will introduce the essential elements of this branch of physics, which are indispensable to analyze the results obtained in this study.

Statistical mechanics is a branch of physics intrinsically related to thermodynamics. The latter is a phenomenological approach that aims to understand the macroscopic properties of systems in equilibrium through energy exchange, either thermally or mechanically. The major achievement of this science was to establish, through experimental means, the laws of thermodynamics. These laws deal with only a few degrees of freedom, specifically the number of variables that can be managed experimentally and measured in a macroscopic setup. On the other hand, statistical mechanics offers a bridge between the macroscopic and microscopic realms of systems in equilibrium by employing a probabilistic approach that considers a large number of degrees of freedom [36].

3.1 The Microcanonical Ensemble

Statistical mechanics approach considers the study of a large collections of systems, each composed of $N \gg 1$ particles, that share a macroscopic feature such as energy or temperature, but prepared considering different configurations in its phase space. Specifically, the microcanonical ensemble considers a large collection of mechanically and adiabatically isolated systems that share the same internal energy E.

Microstates corresponds to a point $\mu(t)$ in the $6N$-dimensional phase space $\Gamma = \prod_{i=1}^{N}\{\vec{q_i}, \vec{p_i}\}$ which evolves following the canonical equations of Hamilton for $\mathcal{H}(\mu)$. In the microcanonical ensemble all the microstates are confined to the surface $\mathcal{H}(\mu) = E$ in the phase space, and the basic postulate of statistical mechanics establish that all the microstates of the energy surface of a closed system can be assumed with equal probability. This means that if $\Omega(E)$ are all the microstates available for the energy E, then the equilibrium probability distribution of microstates is given by:

$$p_E(\mu) = \frac{1}{\Omega(E)} \cdot \begin{cases} 1\ , & \mathcal{H}(\mu) = E \\ 0\ , & \mathcal{H}(\mu) \neq E \end{cases} . \tag{3.1.1}$$

Then, the macroscopic properties of a given system are obtained by taking the ensemble average $\langle \mathcal{O} \rangle$, which is calculated as:

$$\langle \mathcal{O} \rangle = \int \mathcal{O}(\mu)\ p_E(\mu) d\Gamma \tag{3.1.2}$$

where the integral is taken over all the microstates on the phase space.

3.2 Ergodic Hypothesis

In the basic postulate of statistical mechanics, as reflected in Equation 3.1.1, we make a significant assumption by stating that all microstates at a certain energy are equally likely. This assumption is closely related to *ergodic hypothesis*.
A system is said to be ergodic if, for any initial point in the phase space, the trajectory followed by this point eventually passes arbitrarily close to every other point on the constant energy surface. This implies that, over time, every accessible region of the constant energy surface will be explored by the trajectory of any initial point [37]. The main consequence of this hypothesis is that time averages are equal to ensemble averages in the microcanonical ensemble. This allows us to establish that the ensemble average effectively will measure the equilibrium properties of the system independent of the time.

3.3 Correlation Functions

The microcanonical ensemble described in Section 3.1 gives us a path to compute macroscopic quantities. However, *correlation functions* allow us to access the microscopic realm of dynamics. These functions are essential tools for analyzing the microscopic dynamics in physical systems. For instance, magnetization is a macroscopic quantity that emerges from spin-spin interactions. These interactions can be quantified at the microscopic level by the spin-spin correlation function between sites i and j, defined as:

$$C(\vec{r_i}, \vec{r_j}) = \langle (s_i - \langle s_i \rangle)(s_j - \langle s_j \rangle) \rangle, \tag{3.3.1}$$

where $\vec{r_i}$ and $\vec{r_j}$ are the position vectors of sites i and j, respectively, and $\langle \dots \rangle$ denotes the ensemble average.

In systems with translational invariance, where the mean values of the spins are uniform across the system, the equation simplifies since $\langle s_i \rangle = \langle s_j \rangle = \langle s \rangle$. This allows the correlation function to be rewritten as:

$$C(|\vec{r_i} - \vec{r_j}|) \equiv C_{ij} = \langle s_i s_j \rangle - \langle s \rangle^2. \tag{3.3.2}$$

It is possible to relate the spin-spin correlation with magnetic susceptibility in a specific ensemble configuration. The magnetic susceptibility is proportional to the sum of all spin-spin correlations, reflecting how small-scale fluctuations influence the large-scale magnetic behavior of the system [38]. Furthermore, an important feature of correlation functions is their correlation length ξ, which measures the distance over which the correlation of a physical property persists. This metric is crucial for understanding the scale at which interactions within the system remain significant.

3.4 Phase Transitions

Phase transitions are changes in a thermodynamic system from one state of matter to another. These changes occur under specific conditions, known as critical conditions. In these conditions a small change in a control parameter (e.g., temperature) causes a sharp change in a measurable physical property, known as the order parameter (e.g., magnetization). These changes can be discontinuous (Figure 3.1(a)) or continous (Figure 3.1(b)). What is remarkable is that, outside of these critical conditions, the same change, or even a larger one, in the control parameter would only produce a minor fluctuation in the physical property [39].

In equilibrium, macroscopic properties of a system can be determined through thermodynamic potentials. The Gibbs potential, G, is particularly useful for calculating properties of equilibrium states by considering thermal and mechanical changes in the system. During a phase transition, a physical property undergoes a sharp change, which is associated with the derivatives of G. According to the Ehrenfest classification, phase transitions are divided into two types, based on the behavior of the derivatives of G. If the first derivative of G is discontinuous, it is a first-order phase transition. Examples of first derivatives of the Gibbs potential are the entropy S, volume V and magnetization M:

$$S = -\left(\frac{\partial G}{\partial T}\right)_P, \quad V = \left(\frac{\partial G}{\partial P}\right)_T, \quad M = -\left(\frac{\partial G}{\partial H}\right)_T. \tag{3.4.1}$$

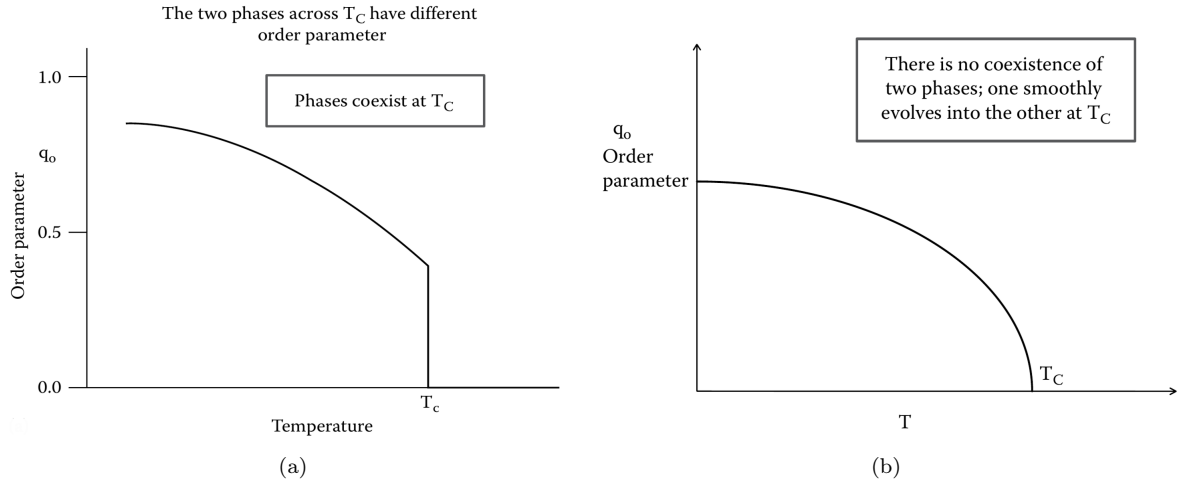

Figure 3.1: Phase diagrams of first and second order phase transitions in (a) and (b) respectively, characterized by an order parameter q_0 and the temperature as control parameter. Notice the discontinuous change of q_0 at T_c in (a), and the continous change in (b). Source: Chaddah, 2017, p.37-38.

Where T represents the temperature, P the pressure, and H the magnetic field, respectively.

On the other hand, if a second or higher-order derivative is discontinuous, the transition is of n-th order, where n is the order of the first discontinuous derivative found in the iterative process. Some examples of second derivatives of the Gibbs potential are specific heat C_p, compressibility κ and magnetic susceptibility χ:

$$C_P = -T\left(\frac{\partial^2 G}{\partial T^2}\right)_P, \quad \kappa_T = -\frac{1}{V}\left(\frac{\partial^2 G}{\partial P^2}\right)_T, \quad \chi = -\left(\frac{\partial^2 G}{\partial H^2}\right)_T. \tag{3.4.2}$$

It's important to highlight that while Ehrenfest's classification is mathematically precise, it encounters phenomenological and experimental challenges for phase transitions with $n > 2$ due to the inherent difficulties in measurements and the possibility that changes between phases may not be apparent. Moreover, in first-order transitions, it does not establish the existence of widely measured metastable states [39]. Thus, we can generally establish the following comparative in Table 3.1 between first and second-order transitions, which are the most commonly measured and studied over the years:

Characteristic	**First Order Transition**	**Second Order Transition**
Order Parameter	Discontinuous	Continuous
Latent Heat	Present with constant value	No latent heat; continuous during transition
Phase Coexistence	Yes	No phase coexistence
Correlation Length	Finite	Diverges
Metastable States	Yes	No

Table 3.1: Comparison of the main features of First and Second Order Phase Transitions at the critical point. Source: Own Elaboration.

Chapter 4

Bridging Lattice Models and Cellular Automata

When we read the definition of cellular automata given in Chapter 2, it is unavoidable to think in *lattice models*. Lattice models are theoretical representations of physical systems in which space is discretized, with interactions occurring at fixed points on a lattice, typically with their nearest neighbors [40].
One of the earliest solved and most widely used lattice models is the Ising model [41]. This model consists of a d-dimensional lattice with L nodes. Each node has a particle characterized by a discrete variable, referred to as the *spin* (considering the classic sense of the concept), which can take values $s_i = \pm 1$. The model aims to study the collective alignment of these spins, resulting from spin-spin interactions and external disturbances. Its primary application is to model the behavior of magnets, and it is governed by the following Hamiltonian:

$$\mathcal{H} = -\frac{1}{2} \sum_{<i,j>}^{N} J_{ij} s_i s_j - B \sum_{i}^{N} s_i \ . \tag{4.0.1}$$

In this expression, J_{ij} represents the coupling factor between spins, B is an external magnetic field, and the notation $\sum_{<ij>}$ indicates summation over nearest-neighbor interactions. A central aspect of this model is its ability to capture the transition of a magnet from ferromagnetic to paramagnetic behavior at the Curie temperature. Thus, temperature T serves as a control parameter, while the magnetization M is the order parameter, which characterizes this phase transition. Using eq.(4.0.1) and principles of statistical mechanics, we can derive thermodynamic observables, however, this is a challenging task. The Ising model has been solved only in the one-dimensional case [41], where the magnetization is zero without an external field, and in the two-dimensional case [5, 6], where magnetization emerges from nearest-neighbors interaction at temperatures $T < T_C$, where T_c is the critical temperature. These

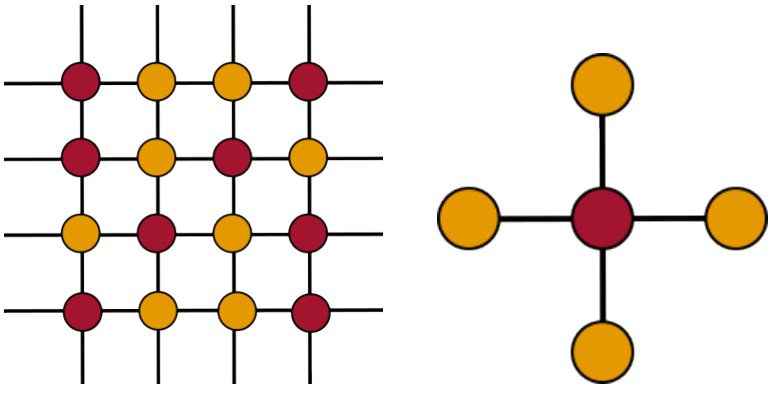

(a) (b)

Figure 4.1: (a) A 4×4 Ising model system with $L = 16$ nodes. The symbol (●) indicates a spin down (-1) while (●) indicates a spin up $(+1)$. (b) Example of Nearest neighbors of a spin down. Source: Own Elaboration

analytical results reveal that spins align in specific directions, showing a behavior governed only by spin-spin interactions. Therefore, simulating the Ising and Ising-type models is essential to gain insights into these phenomena and efficiently explore various models.

Despite the apparent similarities between the definitions of cellular automata and lattice models, their underlying differences are profound. Lattice models represent a discretization of physical systems, aiming to study idealized scenarios. In contrast, cellular automata offer a novel approach to examining nature using logical algorithms, rather than Hamiltonians. Hence, even though lattice models bear a resemblance to cellular automata in their discrete nature, characterizing the latter can be challenging due to the lack of parameters in its simulations.

4.1 An Ising Model Cellular Automaton: The Q2R Model

Edward Fredkin was one of the pioneers in bridging the gap between cellular automata and physics. He provided a mathematical foundation that allowed the construction of cellular automata systems with universal capabilities, incorporating concepts from mathematics and physics, such as invertible and conservative quantities [42]. Building on this logical framework, Gerard Vichniac introduced the Q2R cellular automaton to simulate the Ising model [7], and Yves Pomeau identified a conservative energy-like quantity that characterizes its dynamics [12].
The Q2R model is a conservative and reversible cellular automaton, which is reflected in its phase space composed of limit cycles and fixed points (see Figure 4.2). Its reversibility indicates that the system's

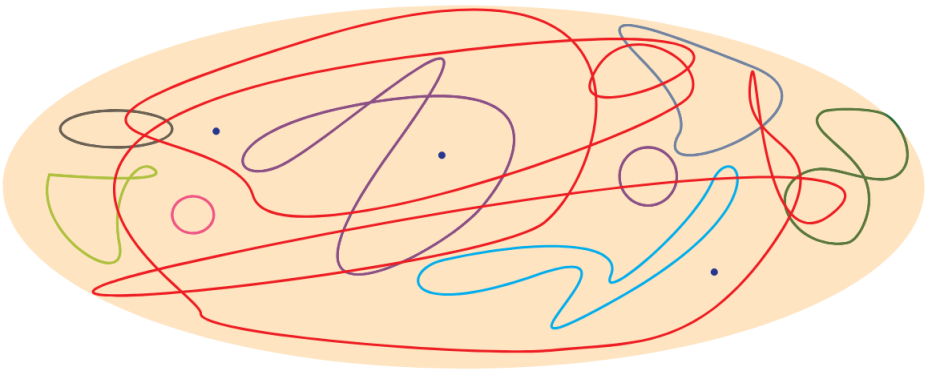

Figure 4.2: Phase space considering constant energy composed of cycles and fixed points. Source: Urbina, 2017, p. 33.

rule is deterministic both forward and backward. For example, a given state at time t, considering its neighbors, leads to a unique state at $t+1$. Conversely, for every state at $t+1$, there exists a unique preceding state at t that resulted in it. This reversibility is signified by the letter "R" in its name. The letter "Q" is derived from the French word for the number 4, *quatre*, which denotes its neighbor interaction using the von Neumann neighborhood. The numeral "2" indicates that it's a *second-order* cellular automaton, this means that to determine a state, say at $t+1$, one must be aware of the cell's state at $t-1$, and its neighbors' state at t. As we can see in its rule of evolution in 4.1.1 [43]:

$$s_k^{t+1} = s_k^{t-1}\phi\left(\sum_{i\in V_k} s_i^t\right) \ , \tag{4.1.1}$$

where s_k^t is one of the two states availables in the Ising model, V_k is the von Neumann neighborhood with periodic boundary condition and, if we denote $x = \sum_{i\in V_k} s_i^t$, the function ϕ is such that

$$\phi\left(x\right) = \begin{cases} +1 \ , & \text{If} \quad x \neq 0 \\ -1 \ , & \text{If} \quad x = 0 \end{cases} \ . \tag{4.1.2}$$

Regarding the simulation of the Ising model, it has been demonstrated that the Q2R cellular automaton exhibits behavior consistent with theoretical expectations in both one-dimensional and two-dimensional cases. Notably, the two-dimensional Q2R undergoes a phase transition around a critical

energy $E_c \approx -\sqrt{2}$ [43, 14], mirroring the Ising model [5, 6] (see Figure 4.3). In more recent works Urbina

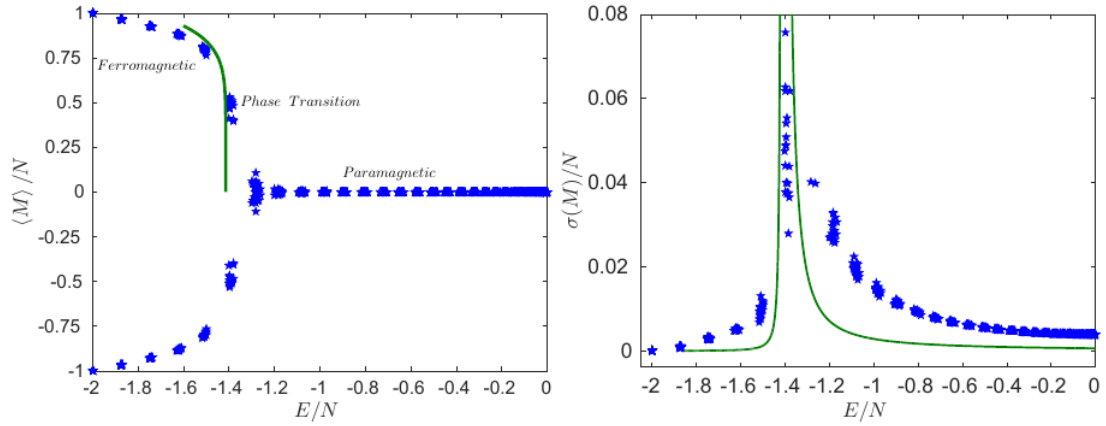

(a) (b)

Figure 4.3: Phase diagram of average magnetization $\langle M \rangle / N$ versus the energy E/N. One can see regions where the system shows ferromagnetic and paramagnetic behavior, for a given initial energy, as well as the critical regime. Figure (b) represents the standard deviation of magnetization versus energy. The continuous line represents the well-known statistical mechanics for the Ising model: $M/N \approx 2^{5/16}(\sqrt{2} + E/N)^{1/8}$. Source: Urbina, 2017, p.30.

and Rica developed a master equation approach that captures the properties of the Q2R model both in equilibrium and out of equilibrium [15]. It has also been studied in the three-dimensional scenario adding different coupling factors, where three different phases are distinguished [17]. Moreover, given its dynamical properties, researchers have approached the model considering the periods of the orbits in the phase space, where one of the results is that there is a critical energy at which the periods in its evolution are beyond the simulation time, and the global period of the system grows exponentially depending on the size of the lattice [13]. On the other side, using the reversibility of the model, the orbits of the phase space of the Q2R model were classified into four distinct categories based on topological characteristics. Through this analysis, it was demonstrated that any configuration of the Q2R belongs to one of these four categories and provides a detailed description of each one [16].

Chapter 5

The Q2R CA Extended to The Potts Model

As previously discussed, the Ising model describe dynamics that account for two possible spin values. However, R. B Potts extended this conception in 1952 to accommodate q different spin values [44]. For $q = 2$, this naturally reduces to the standard Ising model. The Potts model boasts richer dynamics compared to its Ising counterpart and exhibits both first -($q > 4$) and second-order ($2 \leq q \leq 4$) phase transition in the two-dimensional case [45]. And recently has been showed that considering a mean field approach, in the one-dimensional case with $q = 3$, develops first and second order phase transitions [46]. Its Hamiltonian, considering only spin-spin interactions, is given by:

$$\mathcal{H}_{Potts} = -\sum_{<i,j>}^{N} J_{ij}\delta\left(s_i, s_j\right) \tag{5.0.1}$$

Where J_{ij} is the coupling factor between spins, and $\delta\left(s_i, s_j\right)$ is the Kronecker delta:

$$\delta\left(s_i, s_j\right) = \begin{cases} 1\,, & if\ s_i = s_j \\ 0\,, & if\ s_j \neq s_j \end{cases} \tag{5.0.2}$$

Considering more states in the system, despite adding different behaviors on the phase transitions, also increases the potential applications of the model to different situations. For instance, in the simulation of recrystallization and the related annealing phenomena knowing the physical properties of materials is key in the way to characterizing them, and recovery, recrystallization, and grain growth are core elements of the thermomechanical processing to which the materials are subjected [18]. In particular, grain growth is one of the fields in which the Potts model can be applied. A grain is an individual crystal with its own orientation and atomic structure, and a polycrystalline material can be composed of many different grains that interact with each other. On these interactions emerges the macroscopic behavior of a material, thus controlling the grain composition of a material during the grain growth leads to predicting the microstructure, texture, and kinetic properties. In this context, simulations based on the Potts model using Monte Carlo methods have been applied and also have been considered models based on cellular automata [18].
Another example of the application of the Potts model is the cellular cell sorting proposed by Graner and Glazier. Through a Monte Carlo simulation and modifying the Hamiltonian by incorporating different surface energies between cells in its interaction, and an area constraint, they simulate the cell sorting in a tissue composed of three different cell types obtaining clusters formation typically observed in cells [19] (see Figure 5.1).

Following the same path of R. B Potts, Pomeau and Vichniac extended the Q2R cellular automaton to q different states [47]. While this new rule can be extended to encompass any number of q spin values, our focus in this context will be specifically on $q = 3$, whose rule is described in the orginal paper as follows:

Assuming the state S evolves into S', the Q2R-Potts dynamics is depicted in Figure 5.2 proceed as follows:

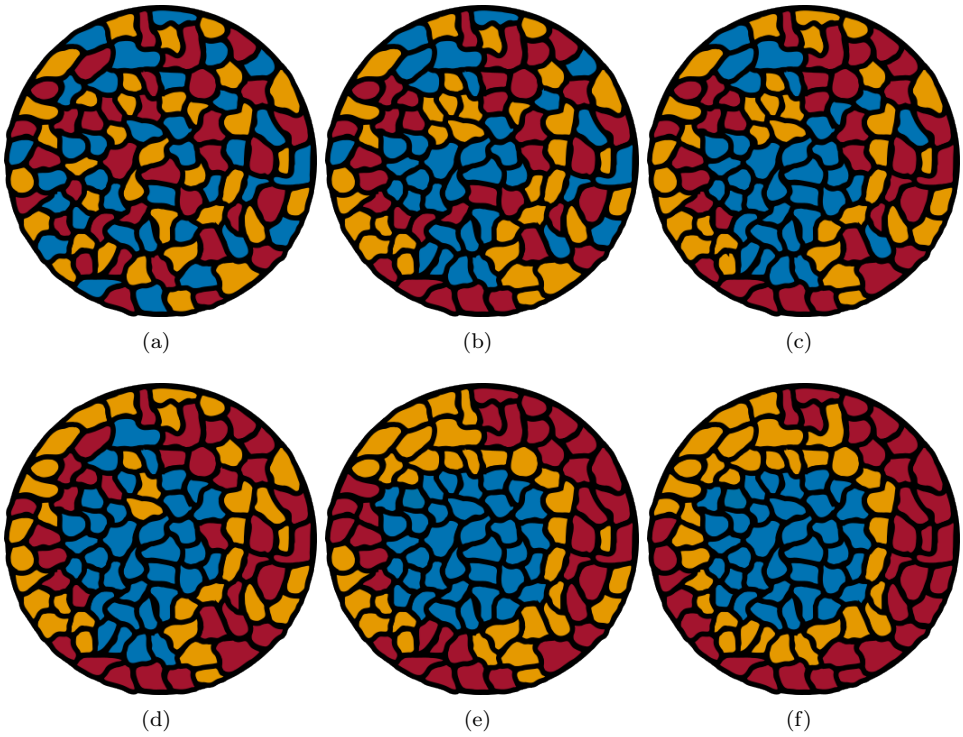

Figure 5.1: Cell sorting evolution through Monte Carlo simulation. In (a) we have the initial configuration randomly distributed and from (b) to (f) we have successive evolution of the process considering different stages showing the pattern and cluster formation. Figure adapted and modified from [19] for aesthetic and pedagogical reasons. Source: Own Elaboration.

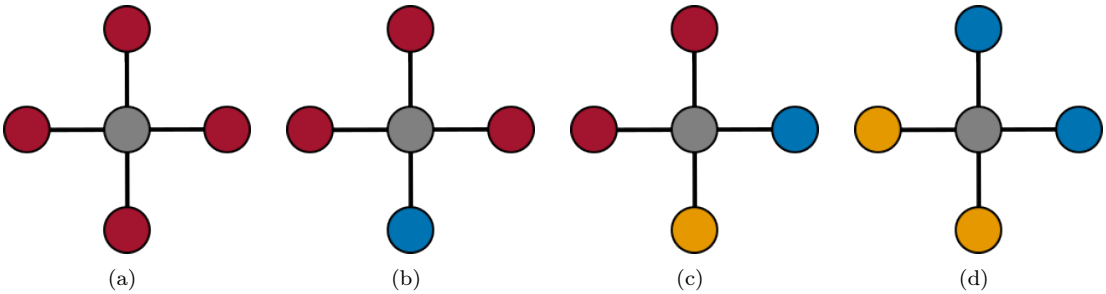

Figure 5.2: The image illustrates the four governing rules for the Q2R-Potts cellular automaton, taking into account all potential configurations of evolution and permutations for a generic central state S.Here, the symbol (●) denotes a spin value of -1, the symbol (●) represents a spin value of 0, and (●) signifies a spin value of $+1$. The symbol (●) stands for a generic state S that can be any of the aforementioned spin values. Source: Own Elaboration.

- In configurations of Figures 5.2(a) and 5.2(b), regardless of the initial central state $S =$ ●, the state evolves such that $S' = S$.

- In Figures 5.2(c) and Figure 5.2(d) we distinguish three subcases. If $S =$ ●, then $S' =$ ●. On the other hand, if $S =$ ● (or ●), then $S' =$ ● (●).

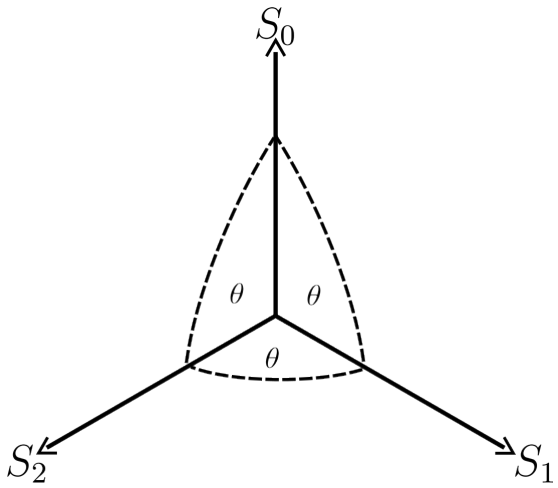

Figure 5.3: Geometrical representation of the Potts model with $q = 3$ states. Each axis S_0, S_1 and S_2 represent a different spin value, and the angle θ is $\frac{2\pi}{3}$ between axis. Source: Own Elaboration.

5.1 Conservative and non-conservative quantities in the Q2R CA

5.1.1 Energy

One of the main features of the dynamic of the Q2R model is its property of reversibility that leads to conservative quantities, which was first identified by Pomeau for the original Q2R model [12], and later formalized for the extended model [47]. Then, we have a conservative energy-like quantity, given by 5.1.1, called in this way for its similarity in the functional form with 5.0.1:

$$E[{s_i}^{t-1}, {s_j}^{t}] = -\frac{1}{V}\sum_{i=1}^{L}\sum_{j\in V_i}\delta\left({s_i}^{t-1}, {s_j}^{t}\right). \tag{5.1.1}$$

In this equation, V it is the quantity of neighbors, ${s_i}^{t-1}$ represent a central state S at time $t-1$, V_i is the set of neighbours of ${s_i}^{t-1}$ at time t, and $\delta\left({s_i}^{t-1}, {s_j}^{t}\right)$ is the Kronecker delta (eq.5.0.2).

5.1.2 Magnetization

The hamiltonian 5.0.1 has an intrinsic symmetry that can be reflected by a hypertetrahedron in $q-1$ dimension [45], then for $q = 3$ we have the two-dimensional projection of a tetrahedron, as we can see in Figure 5.3, where each axis represents a specific spin value S_0, S_1, and S_2. Considering the space formed by the three spin values, we can quantify the magnetization by considering all the spin orientations in the system and calculating a resultant vector with these. So, if $n_p(t)$ represents the density of states in each direction at time t, the magnetization can be expressed as:

$$M(t) = \frac{1}{L}\left|\sum_{p=0}^{2} e^{i\cdot\theta_p}\cdot n_p(t)\right| \tag{5.1.2}$$

Where the angle θ_p is the angle between a fixed axis (e.g. S_0) and the other two, and is given by:

$$\theta_p = \frac{2\pi p}{3},\ p = 0,\ 1,\ 2. \tag{5.1.3}$$

This quantity is not conserved under the dynamics of the Q2R model, but it plays a crucial role in quantifying how a preference for one state over others is established during the system's evolution.

5.1.3 Example of the Q2R-Potts dynamics

In Figure 5.4 the rules of the Q2R-Potts cellular automaton are applied to a two-dimensional system. Furthermore, we can calculate the energy and magnetization of the system as follows:

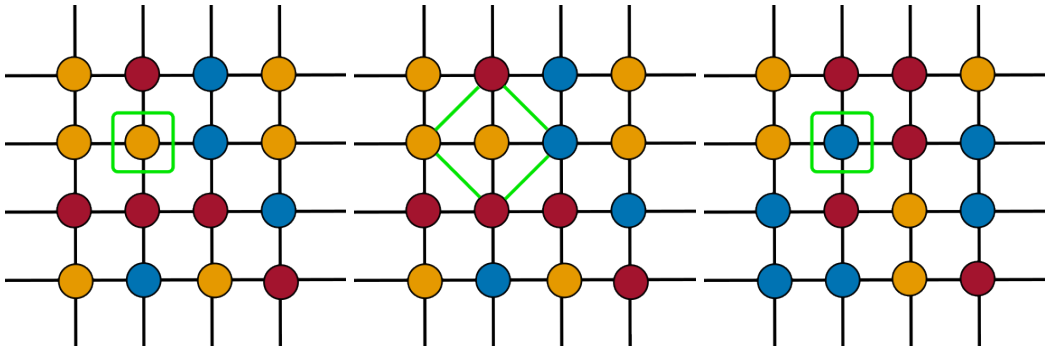

(a) x_k^{t-1} (b) x_k^t (c) x_k^{t+1}

Figure 5.4: Figure illustrates the dynamics of the Q2R-Potts cellular automaton on a two-dimensional square lattice with dimensions $L = 4 \times 4$, taking into account periodic boundary conditions. For simplicity, it has been assumed that the matrices of states at times t and $t-1$ are identical as an initial condition. In (a), we highlight a specific state inside a green rectangle. Moving to (b), the neighbors of this particular state are identified and connected with lines. The evolution rules, as previously defined, are then applied, resulting in the state showcased within the green rectangle in (c). It's important to note that all states within the lattice undergo updates concurrently. Source: Own Elaboration.

- **Energy example:** First we are going to compute the energy associated with the state inside the green rectangle in Figure 5.4(a) to show the process:

$$\begin{aligned} E_{rectangle} &= -\frac{1}{4}\left(\delta\left(\bullet,\bullet\right) + \delta\left(\bullet,\bullet\right) + \delta\left(\bullet,\bullet\right) + \delta\left(\bullet,\bullet\right)\right) \\ &= -\frac{1}{4}(0+0+0+1) \\ &= -\frac{1}{4} \end{aligned}$$

  And summing over all states we obtain:

$$E^t_{Lattice} = -\frac{9}{2}\ ,$$

  To calculate the energy at time $t+1$, consider the states in Figure 5.4(c) as the neighbors configuration and the configuration of states corresponds to Figure 5.4(b). From this, we can notice that this value is:

$$E^{t+1}_{Lattice} = -\frac{9}{2}\ ,$$

  showing the conservation of the energy.

- **Magnetization example:** On the other hand, the magnetization at time t is:

$$\begin{aligned} M(t) &= \left|5 \cdot e^{i\cdot\theta_0} + 4 \cdot e^{i\cdot\theta_1} + 7 \cdot e^{i\cdot\theta_2}\right| \\ &= \left|5 + 4 \cdot e^{\frac{2\pi}{3}} + 7 \cdot e^{\frac{-2\pi}{3}}\right| \\ &= \sqrt{7} \end{aligned}$$

  While at time $t+1$ we have:

$$\begin{aligned} M(t+1) &= \left|5 \cdot e^{i\cdot\theta_0} + 6 \cdot e^{i\cdot\theta_1} + 5 \cdot e^{i\cdot\theta_2}\right| \\ &= \left|5 + 6 \cdot e^{\frac{2\pi}{3}} + 5 \cdot e^{\frac{-2\pi}{3}}\right| \\ &= 1 \end{aligned}$$

Through this example, we can notice that the magnetization changes over time as the states evolve and change their values. While the energy is conserved under the same dynamics.

Chapter 6

The One-dimensional Q2R-Potts CA

To comprehensively grasp the dynamics of the Q2R-Potts cellular automaton, it is crucial to delve into the interplay between its microscopic properties, such as cluster formation, and macroscopic observable like magnetization and energy. With these objectives in mind, the subsequent sections develop the one-dimensional Q2R-Potts CA and its main results.

6.1 The One-dimensional Model

To analyze the Q2R-Potts model, we adapted its original two-dimensional lattice definition to a one-dimensional chain (see Figure 6.2). This adaptation still maintains the periodic boundary conditions as we can see in Figure 6.1 and our exploration encompassed system sizes of $L = 6$, $L = 256$, $L = 512$ and $L = 1024$. The one-dimensional rule is summarized in Table 6.1:

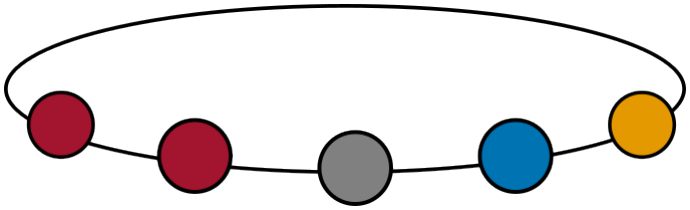

Figure 6.1: The periodic boundary conditions can be visualized as particles arranged on a circle. Source: Own Elaboration.

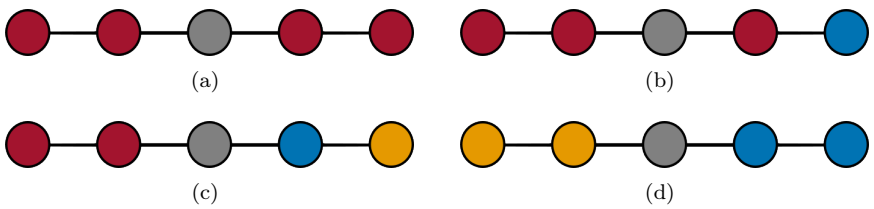

Figure 6.2: Adaptation of the rules from Figure 5.2 to the one-dimensional case, taking into account all potential configurations of evolution and permutations for a generic central state S. The symbol (●) denotes a spin value of -1, the symbol (●) represents a spin value of 0, and (●) signifies a spin value of $+1$. The symbol (●) stands for a generic state S that can be any of the aforementioned spin values. Source: Own Elaboration.

V_k	S_k^{t-1}	S_k^{t+1}
$aaaa$	x	x
$aaab$	x	x
$aabb$	a	b
$aabb$	b	a
$aabb$	c	c
$aabc$	a	a
$aabc$	b	c
$aabc$	b	b

Table 6.1: Summary of the evolution rule for the one-dimensional Q2R-Potts Cellular Automaton (CA). V_K represents the set of neighbors at time t for the state S_k, and S_k^{t+1} denotes its subsequent evolution. The symbols a, b, and c represent specific states, while x stands for a generic state that can be any of the aforementioned. Each set of neighbors takes into account all possible permutations of both states and positions. Source: Own Elaboration.

6.2 Initial conditions

Given the second-order nature of the cellular automaton, initial conditions were set for both the state configurations and their neighbors at $t = 0$, given a phase space composed of $\Omega = 3^{2L}$ possible configurations.

6.2.1 Phase Space Exploration for $L = 6$

For a chain of length L, there are 3^L different configurations, where each can be represented by a number from 0 to $3^L - 1$ in a decimal base, but since we are considering three states, by a transforming from the decimal base to a balanced ternary base we can map all numbers to a specific configuration in a chain of length L.

A ternary base, like any numerical base, seeks the unambiguous representation of numbers, including both natural and negative integers, by using powers of the number 3 and summing them together. The usual coefficients in a ternary base are 0, 1, and 2. However, in a balanced ternary base, symmetry is exploited by using -1, 0, and +1 as coefficients. This choice allows for a more centered representation of numbers, evenly distributing both positive and negative values around zero. Thus, any integer can be represented by the sum of powers of 3, using the aforementioned coefficients. For example, the number -104 in the balanced ternary base corresponds to $1 \cdot 3^0 + 1 \cdot 3^1 + 0 \cdot 3^2 + (-1) \cdot 3^3 + (-1) \cdot 3^4 + 0 \cdot 3^5$, and this is mapped to the configuration $(1, 1, 0, -1, -1, 0)$ in a chain of length 6. Where each element is a factor in the sum of the successive powers of 3 from 0 to $L - 1$.

Following the aforementioned process, we built the $3^6 = 729$ state configurations, and for each, we considered each of the other 729 configurations corresponding to the neighbors, visiting thus the entire phase space composed of $3^{12} = 531,441$ configurations.

6.2.2 Phase Space Exploration for Larger Chains

For $L = 256$, $L = 512$, and $L = 1024$, we define y^t and x^t as matrices representing states and their neighbors, at time t, respectively. Where y^t is a change of variables such that $y^t = x^{t-1}$.

Then, we explored the phase space composed of the following initial conditions:

$$y^{t=0} = x^{t=0} = F(p, r)$$

Where $F(p, r)$ is a probability function given by:

$$F(p,r) = \begin{cases} -1 & \text{with probability } p, \\ 0 & \text{with probability } (1-p)r, \\ +1 & \text{with probability } (1-p)(1-r). \end{cases} \tag{6.2.1}$$

And with $p, r \in [0.005, 0.6]$ exploring 14.400 configurations.

6.3 Microscopic Parameters

As we mentioned earlier, the macroscopic parameters of the Q2R-Potts cellular automaton are its energy (5.1.1) and magnetization (5.1.2). To quantify its microscopic dynamics, we introduce the notion of a cluster of states and its cluster size distribution. In the one-dimensional case, we define a cluster as a

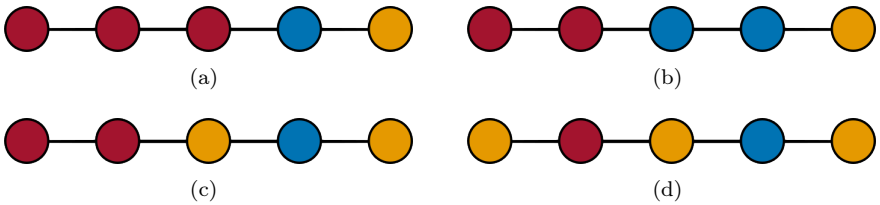

Figure 6.3: One-dimensional system of size five showcasing various cluster configurations. (a) Features a cluster of size 3 for the state (●), and clusters of size 1 for states (●) and (●). (b) Presents clusters of size 2 for states (●) and (●), and a cluster of size 1 for the state (●). (c) Depicts a cluster of size 2 for the state (●), a size-1 for the state (●), and two size-1 clusters for the state (●). (d) Shows size-1 clusters for states (●) and (●). Notably, due to the periodic boundary condition, state (●) forms a size-2 cluster across the boundary, in addition to a size-1 cluster. Source: Own Elaboration.

contiguous sequence of states sharing the same value. Then, a cluster of size l is a sequence of the form $s_0, s_1, s_2, ..., s_l, s_{l+1}$, where $s_1 = s_2 = ... = s_l$, with $s_0 \neq s_1$ and $s_l \neq s_{l+1}$. Notably, due to the system's dynamics, clusters can change over time. To encapsulate this behavior, we describe the cluster size distribution, which represents the frequency of a specific cluster size observed over the entire simulation:

$$f_c(l,t) = \frac{\sum_{t=0}^{\tau} n_l(t)}{\tau \sum_l n_l}. \tag{6.3.1}$$

In this equation, t symbolizes time, and τ stands for the total number of iterations. The subscript l signifies the cluster's size, and $n_l(t)$ represents the number of clusters of size l of a determined state at time t. Finally, the term $\sum_l n_l$ gives a considered state's overall count of clusters.

6.4 Results

6.4.1 Phase Space Classification for $L = 6$

- **First Research Question**

To explore features regarding the reversibility nature and periods of the automaton we considered the case of a chain of length $L = 6$, where the system possesses $3^{12} = 531441$ configurations, and it is partitioned into subspaces of constant energies E and cycles of period T, as shown in Table 6.2. Due to the two-step rule, that considers an initial condition and its neighbors at different time steps, we define a period T as an entire loop of both, the configuration of states and the configuration of the neighbors at the same time. For example, let's consider the following configurations, $s^{t=0} = (1,1,1,1,1,1)$ and $s^{t=1} = (0,0,0,-1,-1,0)$. For this case, the energy is $E = 0$ and its period it's $T = 2$ that can be identified as a symmetric cycle according to [16], due to the alternance between configuration of states and configuration of neighbors (see Figure 6.4(a)). A period $T = 4$ occurs with the initial conditions $s^{t=0} = (0,-1,1,0,0,0)$ and $s^{t=1} = (1,1,0,-1,-1,0)$. Here the energy is $E = -9$ and the dynamic is shown in Figure 6.4(b), where we can observe that its dynamic can be classified as an asymmetric cycle (see theorem 4.10 [16]) because there is no a configuration with its symmetric pairs during the evolution (see Figure 6.4(b)).

For the entire phase space, we can observe in Table 6.2, 21 different values of energy from 0 to -24, and 17 periods. Where the longest period is $T = 60$ associated with $E = -10$, with 2880 different configurations. The highest number of configurations is associated with $E = -8$, hoarding around 19% of the total configurations, and almost a third part of that has a period $T = 36$. On the other hand, period $T = 2$ has the widest variety of energies, specifically 17.

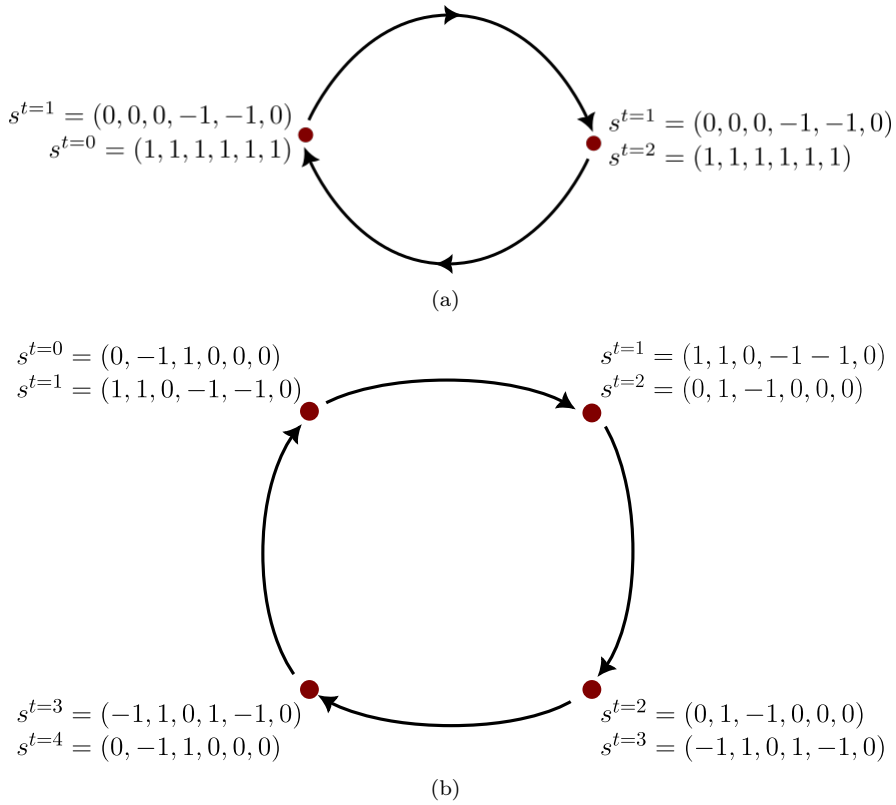

Figure 6.4: Scheme of evolution for symmetric (a) and asymmetric (b) cycles. In (a), the initial configurations $s^{t=0} = (1, 1, 1, 1, 1, 1)$ and $s^{t=1} = (0, 0, 0, -1, -1, 0)$ with an energy $E = 0$ and a period $T = 2$ evolve symmetrically. This symmetry is highlighted by the presence of a composite configuration within the cycle, which contains the permutation of roles between states and neighbors from the initial condition. In (b), the initial configurations $s^{t=0} = (0, -1, 1, 0, 0, 0)$ and $s^{t=1} = (1, 1, 0, -1, -1, 0)$ with energy $E = -9$ and a period $T = 4$ evolve asymmetrically, due to the absence of such permutation between states and neighbors of the initial configuration during its evolution.

Moreover, we have computed the accumulated clusters' configurations for each energy and period (see Table 6.3). For instance, $E = -8$ and $T = 12$ have the widest variety of accumulated clusters' configurations, while the longest period, $T = 60$, has only 4 types of accumulated configurations and is reached with $E = -10$. In the aforementioned, we can see that the maximum cluster's length is $l_c = 3$, and the dynamic is mainly dominated by clusters of size $l_c = 1$ with half of the configurations following the clusters' accumulated frequencies given by Figure 6.5(d).

6.4.2 Larger Chains

To analyze the cases $L = 256$, $L = 512$ and $L = 1024$ we will follow the style of Wolfram, as in Figure 2.3, by qualitatively describing the evolution over time for different energies and, after that, we are going to quantify its macroscopic and microscopic dynamics by using the magnetization and cluster size distribution respectively.
For the Q2R-Potts CA, we have that the behavior of its evolution is strictly related to the energy in the system. Following this, there are three macroscopic behaviors identified which are independent of the chain length (see Appendix A). For this reason, we will focus on $L = 1024$. This length not only reflects a dynamic convergence similar to what is observed in a longer chain but also efficiently encompasses the dynamics of the three states of interest in most of its points, all while significantly reducing computational expenditure in comparison to larger chains. Nevertheless, all the macroscopic study of the other cases will be covered in appendix A.

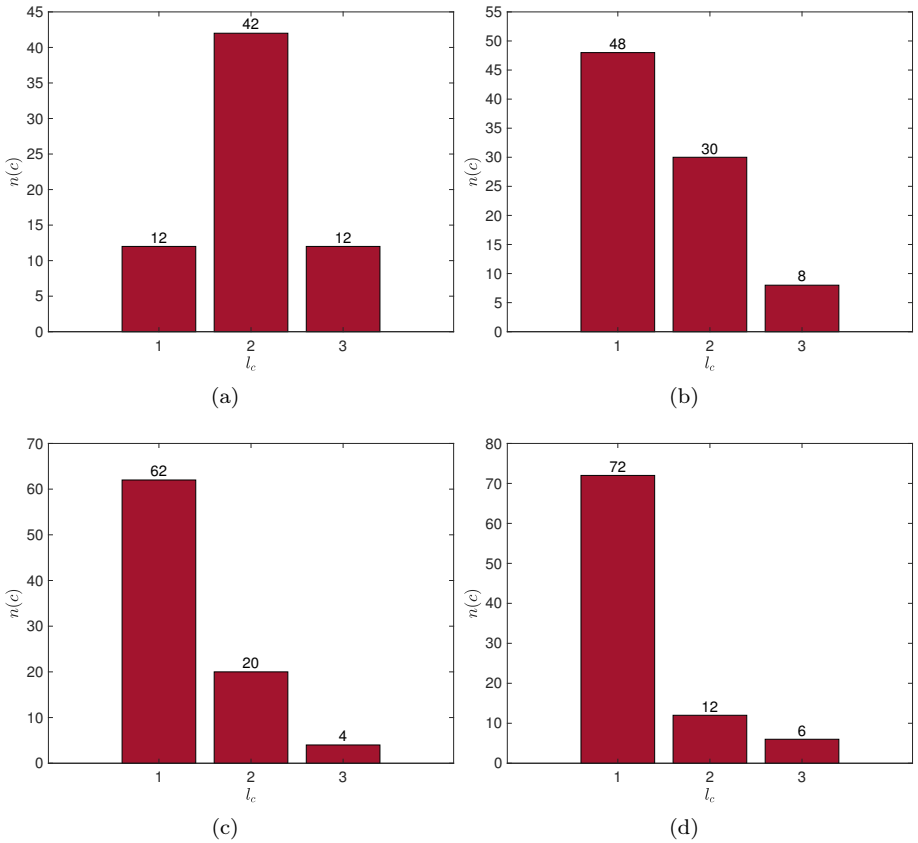

Figure 6.5: All the accumulated clusters' configurations for $T = 60$ and $E = -10$. The x-axis, l_c, represents the length of the cluster, while $n(c)$ is the frequency associated with the entire simulation. From the 2880 that evolves with these distributions of clusters, 240 evolved with the pattern of (a), 480 as in (b), 720 as in (c), and 1440 as in (d). Source: Own Elaboration.

	T																	
E	1	2	3	4	6	8	9	10	12	15	16	20	24	32	36	40	60	$n(T)$
0	6	540	0	0	0	0	0	0	0	0	0	0	0	0	0	0	0	546
-1	0	1008	0	0	0	0	0	0	0	0	0	0	0	0	0	0	0	1008
-2	0	288	0	2160	0	576	0	0	432	0	0	0	0	0	0	0	0	3456
-3	0	1152	0	0	2592	576	0	0	1728	0	0	0	0	0	0	0	0	6048
-4	0	288	0	5688	576	9504	0	0	4608	180	1152	0	0	0	0	0	0	21996
-5	0	144	0	0	2160	5760	0	1440	6912	0	9216	5760	0	0	3456	0	0	34848
-6	0	144	0	4704	1728	14400	0	0	9648	0	6912	11520	10368	0	5184	2880	0	67488
-7	0	0	0	4032	2592	6912	0	0	19008	0	13824	0	0	18432	15552	0	0	80352
-8	18	162	54	8424	1656	11808	0	0	14760	0	18432	5760	8064	0	32832	0	0	101970
-9	0	0	0	2304	2592	6912	0	0	11136	0	18432	0	0	9216	10368	23040	0	84000
-10	72	216	0	2592	4752	6912	0	0	12960	0	18432	2880	4608	2304	6048	0	2880	64656
-11	0	0	0	0	2592	9216	0	2880	12096	0	0	2880	1152	0	0	0	0	30816
-12	0	432	12	6720	432	3168	108	0	8640	0	0	0	0	0	0	0	0	19512
-13	0	576	0	0	432	1152	0	0	1728	0	2304	0	0	0	864	0	0	7056
-14	0	576	0	1224	432	2304	0	0	0	0	576	0	0	0	0	0	0	5112
-15	0	0	0	864	0	0	0	0	0	0	0	0	0	0	0	0	0	864
-16	36	288	36	360	54	576	0	0	0	0	0	0	0	0	0	0	0	1350
-17	0	144	0	0	0	0	0	0	0	0	0	0	0	0	0	0	0	144
-18	0	144	0	0	0	0	0	0	0	0	0	0	0	0	0	0	0	144
-20	0	72	0	0	0	0	0	0	0	0	0	0	0	0	0	0	0	72
-24	3	0	0	0	0	0	0	0	0	0	0	0	0	0	0	0	0	3

Table 6.2: Distribution of the number of configurations by cycles T for a periodic chain of length $L = 6$ according to its energy. Source: Own Elaboration.

	T																
E	1	2	3	4	6	8	9	10	12	15	16	20	24	32	36	40	60
0	1	13	0	0	0	0	0	0	0	0	0	0	0	0	0	0	0
-1	0	7	0	0	0	0	0	0	0	0	0	0	0	0	0	0	0
-2	0	5	0	13	0	4	0	0	2	0	0	0	0	0	0	0	0
-3	0	9	0	0	8	2	0	0	2	0	0	0	0	0	0	0	0
-4	0	7	0	21	5	32	0	0	11	2	7	0	0	0	0	0	0
-5	0	2	0	0	7	12	0	4	10	0	7	3	0	0	2	0	0
-6	0	2	0	21	5	35	0	0	21	0	12	8	9	0	5	3	0
-7	0	0	0	14	8	9	0	0	26	0	11	0	0	8	9	0	0
-8	2	6	3	37	16	26	0	0	39	0	18	8	7	0	21	0	0
-9	0	0	0	9	8	11	0	0	16	0	12	0	0	6	7	8	0
-10	3	4	0	17	15	19	0	0	21	0	25	4	5	4	8	0	4
-11	0	0	0	0	8	11	0	5	15	0	0	2	1	0	0	0	0
-12	0	6	1	30	2	20	1	0	17	0	0	0	0	0	0	0	0
-13	0	4	0	0	2	3	0	0	2	0	3	0	0	0	1	0	0
-14	0	4	0	9	2	11	0	0	0	0	2	0	0	0	0	0	0
-15	0	0	0	4	0	0	0	0	0	0	0	0	0	0	0	0	0
-16	3	7	3	6	2	6	0	0	0	0	0	0	0	0	0	0	0
-17	0	2	0	0	0	0	0	0	0	0	0	0	0	0	0	0	0
-18	0	3	0	0	0	0	0	0	0	0	0	0	0	0	0	0	0
-20	0	3	0	0	0	0	0	0	0	0	0	0	0	0	0	0	0
-24	2	0	0	0	0	0	0	0	0	0	0	0	0	0	0	0	0

Table 6.3: Distribution of the number of different configurations of accumulated clusters by cycles T for a periodic chain of length $L = 6$ according to its energy. Source: Own Elaboration.

Order: $E/L = -0.924$

In the dynamic of the Q2R-Potts CA, we have identified three behaviors. One of them corresponds to the dynamic shown in Figure 6.6 with an energy density $E/L = -0.924$ (energy density goes from -1 to 0). In Figure 6.6(a) we have the pattern formed in the last 5000 time steps, where the dynamic follows the same rules as in Figure 2.3, i.e., each row represents the state of the CA at a given time and the time evolves downward. This energy density is near the minimum available in the system, and we can see a very regular pattern, consisting of parallel flat strips and strips that incorporate periodicity in both the red state and blue state. Also, We can notice a region with triangular structures and the yellow state dominates the dynamic.
To give a quantitative description of the dynamic, we measured the magnetization, which shows very regular fluctuations from $M(t) \approx 0.79$ to $M(t) \approx 0.94$ (see Figure 6.6 (b) and (c)). Although the dynamics of the magnetization look quite regular and periodic, it isn't. We have the fluctuations regions and the type of curves in it very well defined, but each peak and valley shows slight differences with each other.

Disorder: $E/L = -0.506$

The other case easily distinguished is the disordered case. This scenario is completely the opposite of shown in Figure 6.6 because it doesn't show any type of structure that persists over its evolution. In Figure 6.7(a) we can see the last 5000 time steps in an evolution of 1 million steps, which looks quite random and noisy in terms of the states over the configuration. The little structures that one can distinguish are tiny and don't persist nor dissipate over the evolution of the system.
In terms of the magnetization, the fluctuations go from $M(t) \approx 0$ to $M(t) \approx 0.13$, almost the same range ΔM that we saw in Figure 6.6, but without a specific pattern. In this case, the system didn't achieve a period either over the simulation.

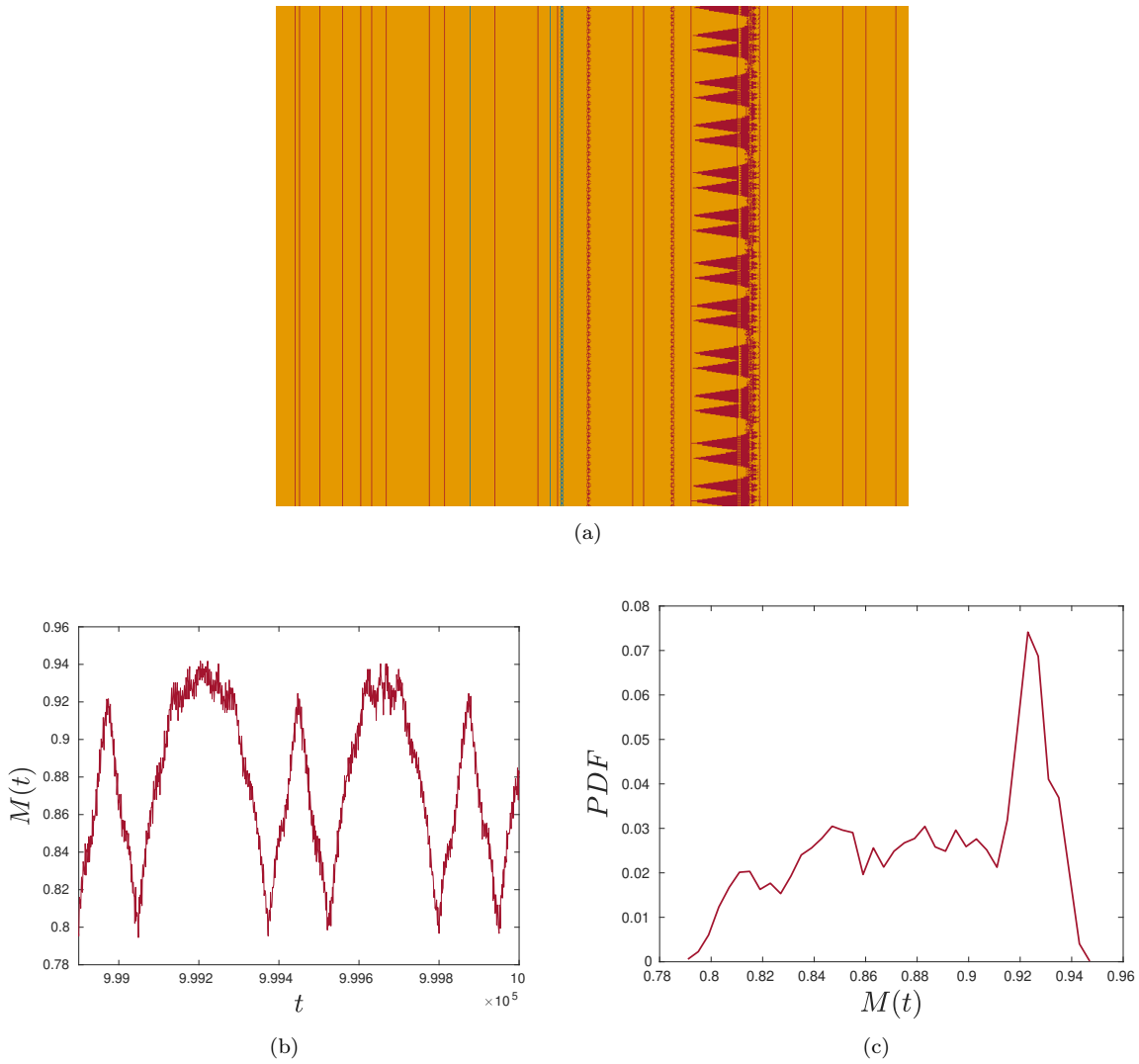

Figure 6.6: Macroscopic dynamic for energy density $E/L = -0.924$. In (a) we have the pattern formed by the Q2R-Potts' evolution rules in the last 5000 steps in a simulation of 2 million time steps. In (b) there is the measurement of the evolution of magnetization over time, and (c) is the probability density function of the magnetization over the entire simulation. Pictures (a) and (b) follow quite regular patterns, but in the total simulation, the system doesn't complete a period. Source: Own Elaboration.

Fluctuations: $E/L = -0.886$

A very interesting behavior emerges for $E/L = -0.886$, where we can distinguish behaviors of order, disorder, and the transition among them for a given initial condition. These give as a result a non-trivial behavior for the entire simulation of this energy density, mainly characterized by big fluctuations.
In Figure 6.8(a) we can observe similar dynamics as in Figure 6.6(a), with periodic and regular linear structures that persist over time, and with a region of fluctuations. In this case, the fluctuations don't follow a regular pattern as in Figure 6.6(a) (triangular structures), and this is captured by the magnetization over time (see Figure 6.8(b)) that doesn't follow a recognizable pattern and fluctuates between $M(t) \approx 0.66$ and $M(t) \approx 0.86$ (overall fluctuation around 5 centesimal units bigger than in the ordered and disordered cases seen earlier).
In Figure 6.8(c) and Figure 6.8(d) we move forward in time and cover the dynamics of 429.600 to 434.600 time steps. The space-time evolution for this time window is something that has elements from Figure 6.6(a) and Figure 6.7(a), with small regions that look quite regular with some periodic structures or clusters, and with thin bands propagating over the dynamic of the system with a noisy distribution of states quite similar to Figure 6.7(a). Besides the behavior previously mentioned, we also can see clusters moving around and crashing with each other creating new forms or disappearing. Although this behavior

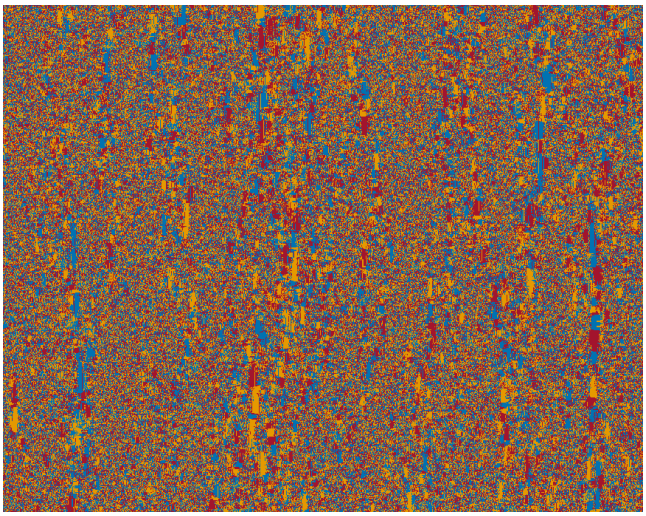

(a)

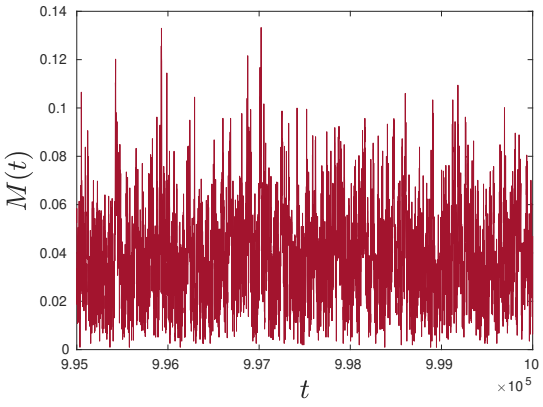

(b)

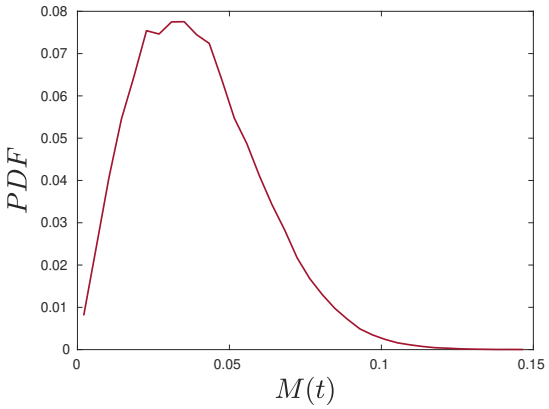

(c)

Figure 6.7: Macroscopic dynamic for energy density $E/L = -0.506$. In (a) we have the pattern formed by the Q2R-Potts' evolution rules in the last 5000 steps in a simulation of 2 million time steps. In (b) there is the measurement of the evolution of magnetization over time, and (c) is the probability density function of the magnetization over the entire simulation. Pictures (a) and (b) look very noisy and don't follow any pattern. Source: Own Elaboration.

looks quite particular and, as a whole, is not at all similar to Figure 6.7(a), however, the magnetization is quite close to 0 (see Figure 6.8(d)) and at times is in the same ranges as Figure 6.7(b). At first glance, the formation of clusters makes the difference between the cases above, and it will become clear later on. Finally, in Figure 6.8(e) and Figure 6.8(f), we have the dynamic restricted between 995.000 and 1.000.000 time steps. In this dynamic, we have a dominant state over the others, in this case, the red state. However, we also can notice big clusters of the other two states, and triangular fluctuating structures that change over time. All the previously discussed give as a result a magnetization that fluctuates irregularly between $M(t) \approx 0.35$ and $M(t) \approx 0.52$ (see Figure 6.8(f)).
In Figure 6.9(a) we have the entire evolution of the magnetization, where we can observe the fluctuations in the system, which are mainly distributed between $M(t) \approx 0$ and $M(t) \approx 0.5$, with some peaks that reach $M(t) \approx 0.7$. This can be seen in the probability density function in Figure 6.9(b). Also, we can see how the individual states are distributed in their probability density function in Figure 6.9(c).

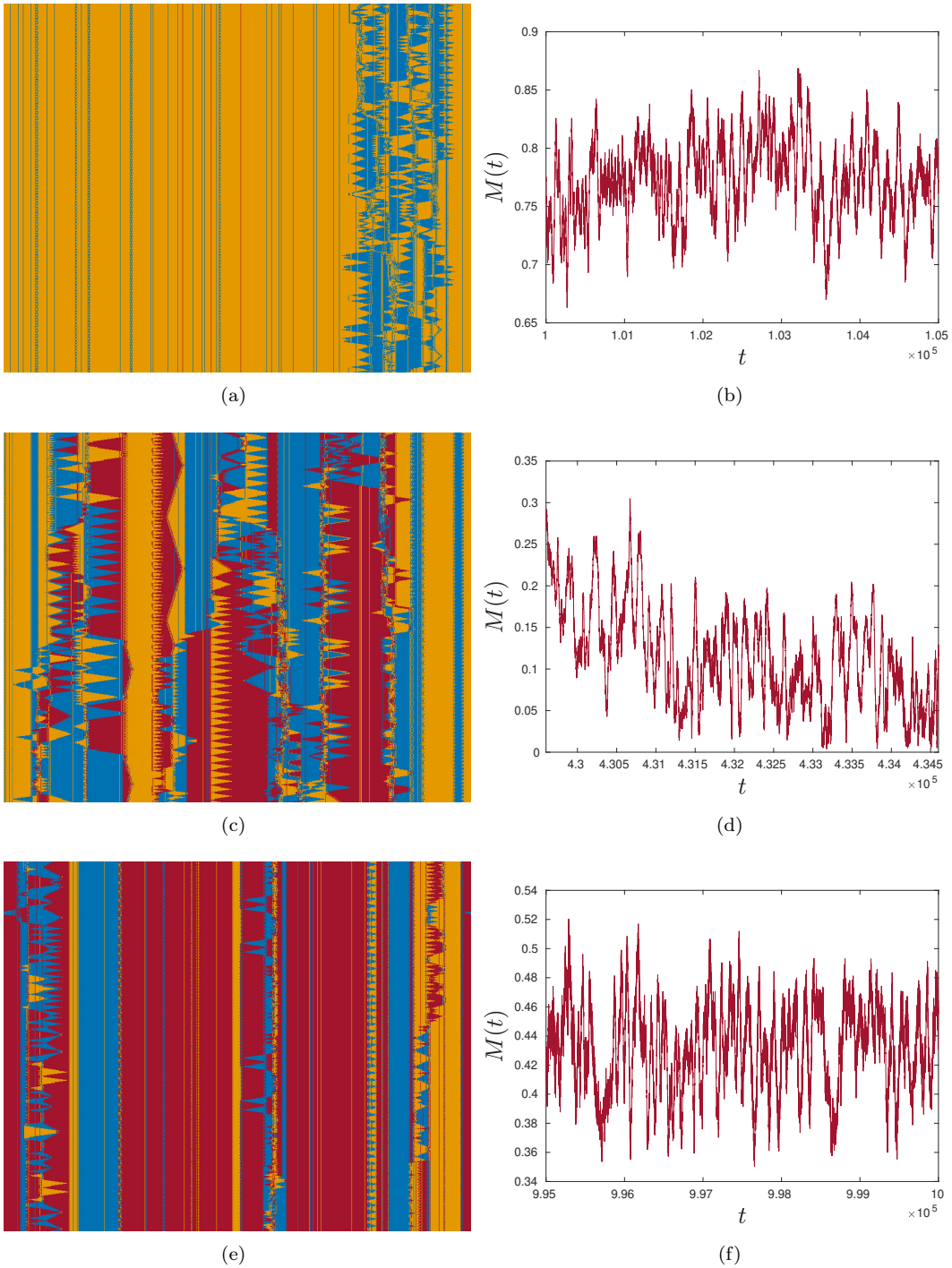

Figure 6.8: Space-time and magnetization evolution of the system for an energy density $E/L = -0.886$ at different times. In figures (a), (c), and (d) we have the different patterns formed at times from 100.000 to 105.000 steps, 429.600 to 434.600 steps, and 995.000 to 1.000.000 steps, respectively. While (b), (d), and (f) show the temporal series of the magnetization associated with (a), (c), and (d) respectively. Source: Own Elaboration.

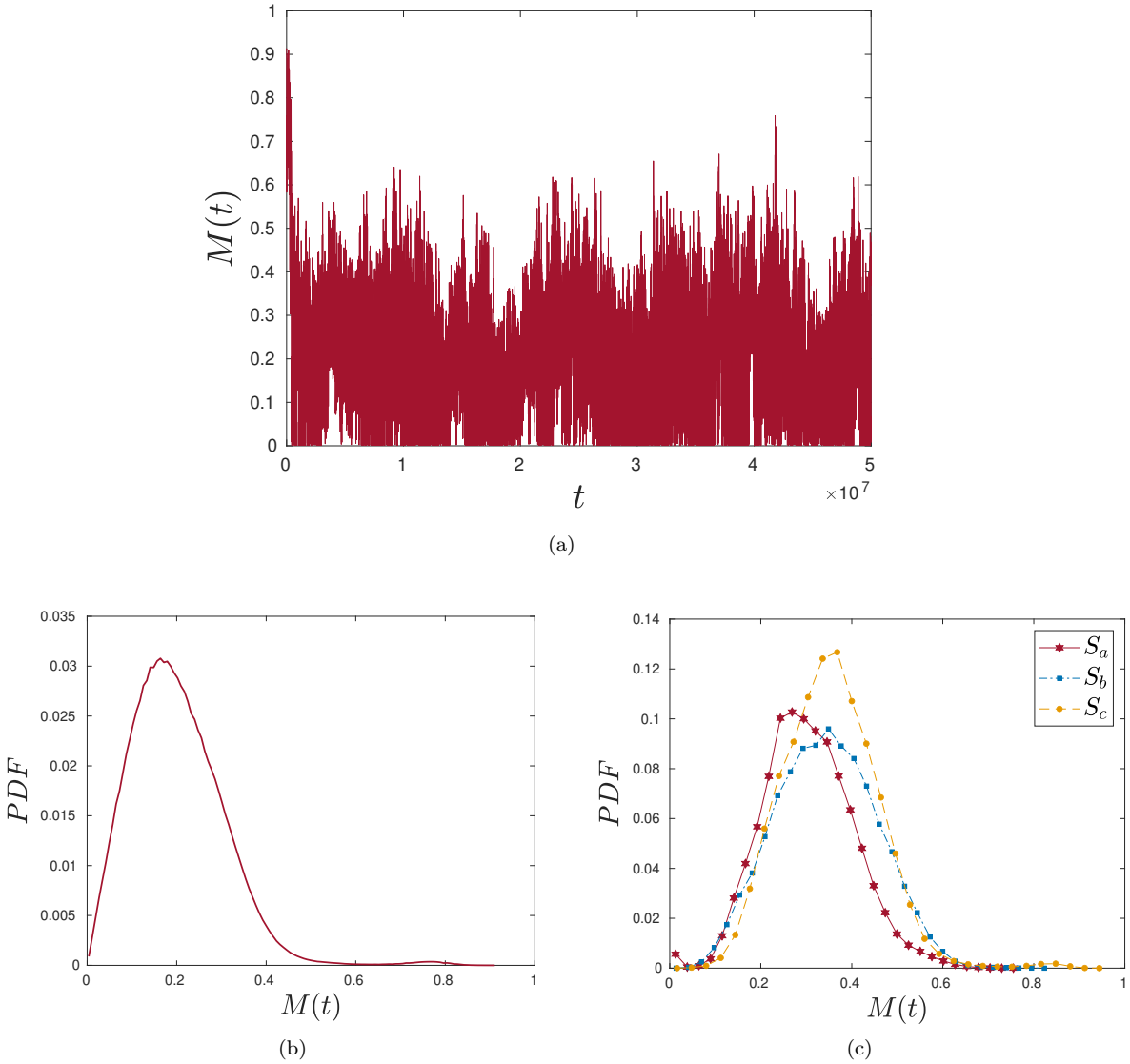

(a)

(b)

(c)

Figure 6.9: Dynamic of the magnetization and probability densities distribution for the energy density $E/L = -0.886$. In (a) we have the temporal series of the magnetization considering fifty million time steps, in (b) we can see the probability density distribution of the magnetization, and in (c) we observe the probability density distribution of the magnetization per state. Source: Own Elaboration.

6.4.3 Macroscopic Dynamics

- **Second Research Question**

Until now, we have seen different dynamics in the one-dimensional Q2R-Potts CA from both a qualitative and quantitative point of view. From the aforementioned study, one of the conclusions that we may state is that the general behavior of the system, and its magnetization, change when we change the energy density E/L. But to answer how exactly changes we built a phase diagram considering the average magnetization $\langle M \rangle$ as the order parameter and the energy density E/L as the control parameter (see Figure 6.10). In Figure 6.10(a), we present the macroscopic description of the system in terms of our

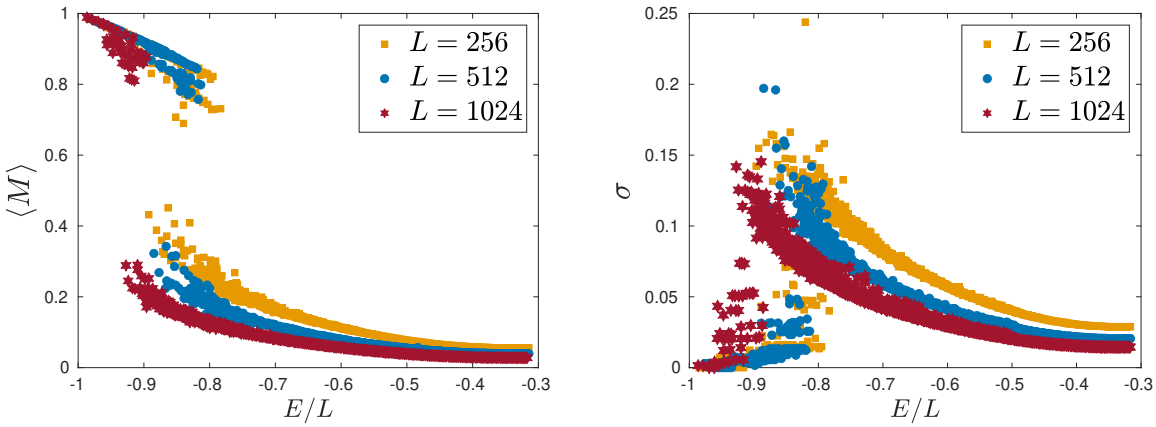

(a) (b)

Figure 6.10: Phase diagrams for chains of length $L = 256$, $L = 512$ and $L = 1024$. In (a) the phase diagram of average magnetization $\langle M \rangle$ versus E/L, and in (b) we have the standard deviation σ versus E/L. Source: Own Elaboration.

chosen order and control parameters. Qualitatively, all the chains studied exhibit similar behavior, and quantitatively, there are no significant differences between the chain of size $L = 1024$ and larger chains. Therefore, our analysis will primarily focus on the chain of size $L = 1024$. When the energy density increases from the lowest energy configuration, the system responds with a consistent decline in magnetization, initially following a linear trend. As the energy density continues to increase, the decrease in magnetization becomes more pronounced while entering a critical region that culminates in a sharp drop in magnetization from $\langle M \rangle \approx 0.8$ to $\langle M \rangle \approx 0.3$. In parallel, the standard deviation increase and reach the maximum value in the critical region $E/L \approx -0.9$ and $E/L \approx -0.8$ (see Figure 6.10(b)). Finally, for energies greater than $E/L > -0.8$, the magnetization and its fluctuations decay exponentially to $\langle M \rangle \approx 0$.

In Table 6.4 we summarize some important values from the phase diagrams in Figure 6.10:

E/L	$F(p, r)$	$\langle M \rangle$	σ
-0.927	$F(0.02, 0.02)$	0.293	0.154
-0.915	$F(0.024, 0.027)$	0.810	0.073
-0.910	$F(0.027, 0.027)$	0.279	0.131
-0.906	$F(0.021, 0.033)$	0.864	0.053
-0.889	$F(0.035, 0.025)$	0.244	0.158

Table 6.4: Parameters and initial conditions for some representative values from Figure 6.10.

In particular, we have that energy densities -0.927 and -0.889 are the highest values in the standard deviation, and the first one is the biggest value of magnetization after the transition. On the other hand, energy densities -0.915 and -0.906 have the lowest magnetization before the transition. Finally, $E/L = -0.910$ has an interesting dynamic presenting large fluctuations.

6.4.4 Microscopic Dynamics

- **Third and Fourth Research Question**

Something that we realized when studying the fluctuations in the dynamic for the energy density $E/L = -0.866$, is that clusters play a key role in it, and by watching figures Figure 6.6(a), Figure 6.8 and Figure 6.7(a), is that the length of clusters, and its evolution are related to the energy density. This is shown in Figure 6.11, where measure the longest cluster in the evolution of the system per energy density, and we can see that in the range $-1 < E/L < -0.9$ the maximum available in the system is mainly dominated by one state (in this case the yellow state). If we go to $E/L \approx -0.9$ we have a maximum cluster growth for all states, peaking around this energy density. And finally for $-0.8 \leq E/L$ we have an exponential decaying of the maximum cluster available per energy density (see Figure 6.11). Notice the similarity between Figure 6.11 and Figure 6.10(b).

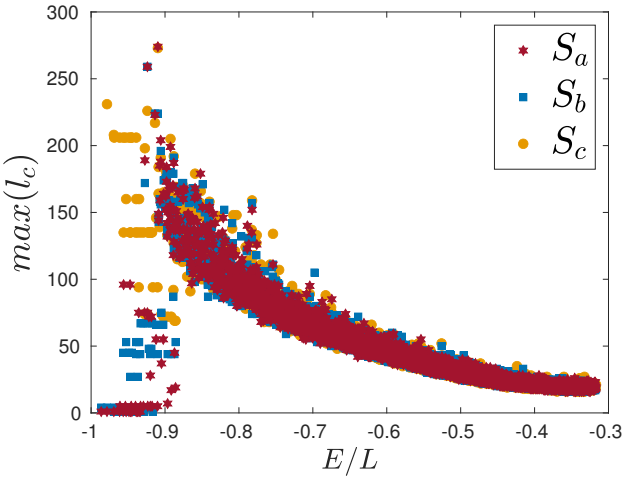

Figure 6.11: Maximum cluster length available in the system for each energy density after 2 million time steps. Source: Own Elaboration.

To understand deeply the distribution of clusters, besides measuring the maximum cluster's length available per energy density, we can access the cluster size distribution to measure with what frequency a specific cluster length appears per energy density after a simulation. So, we followed the same logical process as in the section 6.4.2 by considering the same cases in Figure 6.12. In Figure 6.12(a) we have the ordered case, and we can see that the cluster frequency is mainly dominated by one state, as one can expect by watching Figure 6.6(a). This means that the figure Figure 6.6(a) is representative of the entire dynamic of the system. In Figure 6.12(b) we have the case of fluctuations, and we can notice that different states dominate at different cluster's lengths following a clear exponential tendency, where the maximum length available in the system is $l_c = 266$. By fitting an exponential fit we found that $f_c \sim e^{-0.07}$. Finally, in the disordered case, the exponential tendency is stronger than in the case of fluctuation with an exponent $\lambda = 0.6$, and we can notice that the maximum cluster length for this configuration is $l_c = 30$, which explains the differences between the snapshots Figure 6.7(a) and Figure 6.8(c). With the previous analysis of particular cases, we got light on how the exponent of the exponential fit changes depending on the energy density, and in Figure 6.13 we have the full picture of the qualities of the fit, with the different slopes per energy density and the goodness of fit. In Figure 6.13(a) we can see that the slopes converge to $\lambda \approx -1$, and in Figure 6.13(b), (c) and (d) we can see that while we increase the energy, better and more reliable is the fit

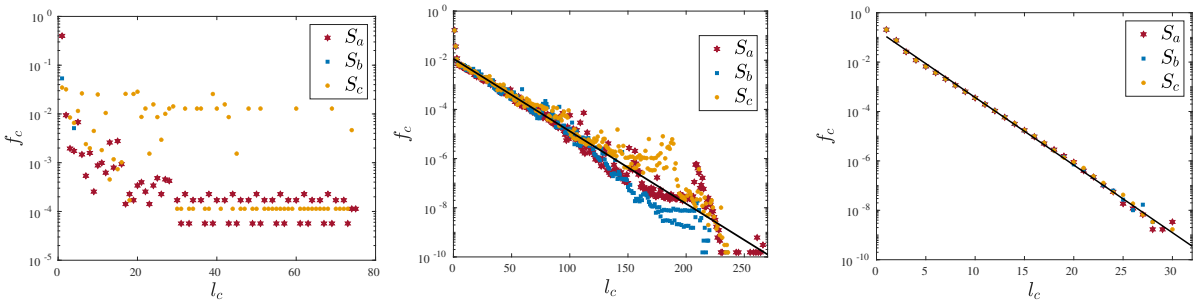

(a) $E/L = -0.924$ (b) $E/L = -0.886$ (c) $E/L = -0.506$

Figure 6.12: Semilog plots for the cluster distribution frequency f_c versus the cluster length l_c. In each plot, black depicted lines indicate least squares fit $f_c \sim e^{\lambda}$. In (a) clusters don't follow an exponential tendency, while in (b) and (c), $\lambda = -0.07$ and $\lambda = -0.6$, respectively. Source: Own Elaboration.

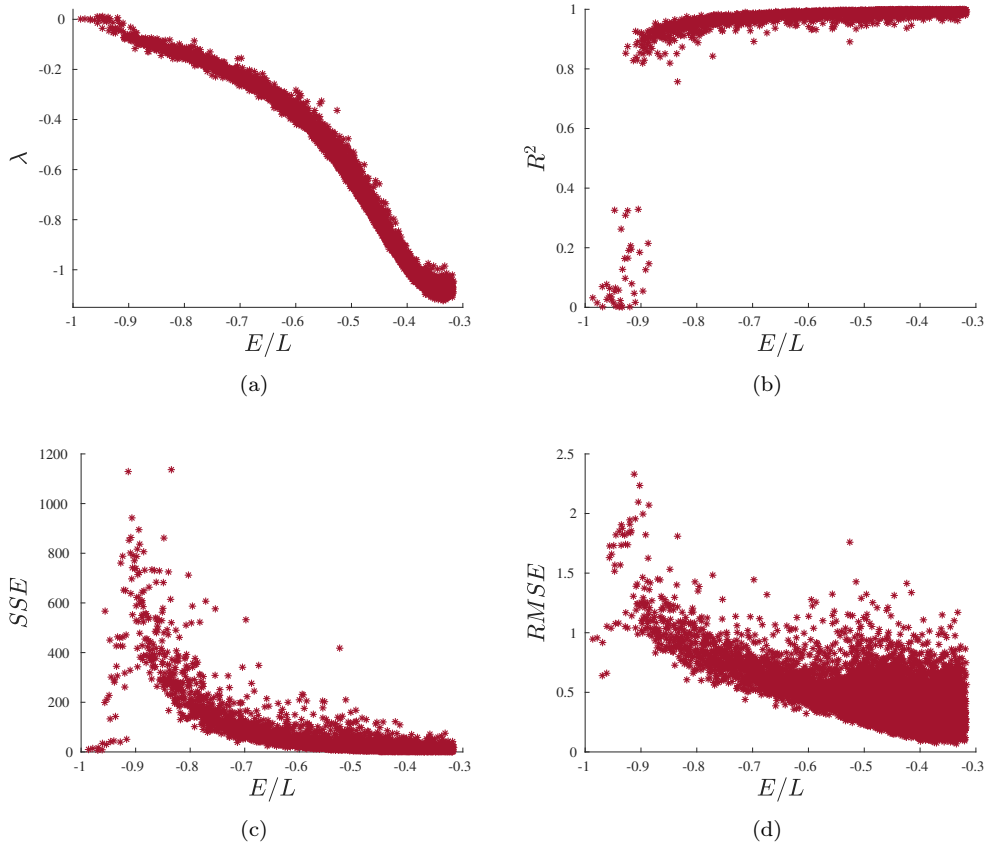

Figure 6.13: Exponent λ as a function of energy density (a), assuming an exponential distribution. The graph also displays various measures of fit quality, including R-squared (R) in (b), Sum of Squared Errors (SSE) in (c), and Root Mean Square Error ($RMSE$) in (d). Source: Own Elaboration.

6.4.5 First-Order Phase Transition in the Q2R-Potts Model

In Figure 6.10(a), the sharp discontinuity in the magnetization indicates that the system develops a first-order phase transition. Moreover, we observed other typical aspects of first-order phase transitions such as coexistence and a reduced size in the clusters of states.

As a non-ergodic system, the Q2R-Potts CA's configurations do not evolve by exploring all the microstates with the same energy. As observed in our phase space study for a chain of length $L = 6$, detailed in Table 6.2 and 6.3. The system, for a given energy, can exhibit different periods and cluster

structures during its evolution (see Figures 6.5 and 6.4). This phenomenon extends to larger systems, such as a chain of length $L = 1024$. In the critical region, around $E/L \approx -0.9$, we observed a phase coexistence where configurations, accessed via different initial conditions at the same energy density, exhibit behaviors either in the ordered phase, or disordered phase for different values of $\langle M \rangle$, as is detailed in Table 6.5:

E/L	$F(p, r)$	$\langle M \rangle$
-0.922	$F(0.024, 0.021)$	0.816
-0.922	$F(0.023, 0.022)$	0.415
-0.907	$F(0.026, 0.028)$	0.834
-0.907	$F(0.024, 0.029)$	0.219
-0.907	$F(0.023, 0.031)$	0.208
-0.898	$F(0.021, 0.038)$	0.858
-0.898	$F(0.033, 0.021)$	0.328

Table 6.5: Parameters and initial conditions for configurations that present coexistence in the critical region.

These findings reveal a different form of phase coexistence inherent to this non-ergodic, conservative, and reversible cellular automaton.

From a microscopic perspective, Figure 6.11 illustrates the behavior of the maximum cluster length available in the system per energy density, which decays exponentially after the transition region and always maintains its size below a third of the system's size, characterizing it as having a short range of correlations through the transition.

Chapter 7

Conclusions

In this thesis, we have delved into the understanding and characterization of the dynamic properties of the Q2R cellular automaton, particularly in its extension to the Potts model with $q = 3$ states, considering both its macroscopic and microscopic dynamics. Through a brief journey into the historical and scientific development of cellular automata, we have explored a vast and diverse field. While we acknowledge that we could not examine many significant contributions in detail, we have managed to link cellular automata with relevant ideas about complexity and computation and integrate them into the conceptualization of lattice models in physics.

A key distinction between lattice models and cellular automata is their capability for quantitative characterization. While the former, emerging directly from physics, possess inherent quantitative predictive power, the latter's quantification is not as direct. In this context, the Q2R automaton stands out for its mathematical formulation, which allows for associating a conservative energy and consequently, an order parameter such as magnetization.

Among the contributions of this work is the complete characterization of the phase space for a chain of length $L = 6$. Our analysis reveals that the phase space of the Q2R-Potts cellular automaton (CA) is divided into subspaces of constant energy, with each energy level associated with a set of configurations that evolve with varying periods and accumulated clusters. This insight was pivotal in understanding the dynamics of clusters. By defining complexity as the coexistence of configurations with different periods, we find that the most complex behaviors manifest in configurations of intermediate energy. Notably, our results demonstrate that no single configuration explores the entire phase space; such a comprehensive exploration would require a period of $T = 531,441$, underscoring the intricate structure of the system's phase space. This fact is particularly noteworthy as it evidences the non-ergodicity of the automaton, revealing that the system does not evolve over time to explore its entire phase space uniformly, a crucial aspect for understanding the underlying dynamics of the Q2R-Potts CA.

After characterizing the phase space for a chain of length $L = 6$, we studied the macroscopic behavior of chains of length $L = 256$, $L = 512$ and $L = 1024$ considering a phase diagram of $\langle M \rangle$ versus energy density E/L. Here, we identified a transition from order to disorder characterized by a discontinuity in $\langle M \rangle$. While this finding may initially be unexpected, as one-dimensional magnetic systems do not exhibit phase transitions when considering only nearest neighbors, as shown by the solution of the one-dimensional Potts model with $q = 3$ states [46], our adaptation of the one-dimensional Q2R-Potts cellular automaton involves a set of four neighbors that ensure the conservation of the dynamic properties of reversibility in the automaton, making this result understandable from that perspective.

Moreover, a key aspect of our research involved analyzing the microscopic dynamics through the lens of cluster formation. Specifically, we plotted the cluster distribution frequency f_c for three different energy densities on a semilog graph. Our findings highlight that the slope following the cluster frequency distribution depends on the energy density governing the configuration, particularly noting self-organization in cases where $E/L > -0.5$. Also, in Figure 6.11, we can observe the longest cluster available in the system per energy density. Intriguingly, these follow a pattern similar to that observed in Figure 6.10(b), indicating a profound connection between the Q2R-Potts cellular automaton and the statistical physics of the system, appropriately connecting magnetic susceptibility and spin-spin correlation [38].

Immediate extensions of this work are to expand this development to two and three dimensions, where our analysis can be key in understanding phase transitions in higher dimensions from a discrete system.

To conclude, this work presents a tool through which we can obtain exact results from a set of logical rules that allows us to conceptually and quantitatively approach emergent phenomena in the Potts model. Thus, the Q2R-Potts model aligns with Von Neumann's vision in designing cellular automata, where they can be used to gain perspective and intuition on a specific problem, but also the Q2R-Potts model allows us to quantify and obtain measurable results.

Bibliography

[1] Pawel Romanczuk and Lutz Schimansky-Geier. Brownian motion with active fluctuations. *Phys. Rev. Lett.*, 106:230601, Jun 2011.

[2] Francisca Guzmán-Lastra, Andreas Kaiser, and Hartmut Löwen. Fission and fusion scenarios for magnetic microswimmer clusters. *Nature Communications*, 7(1):13519, Nov 2016.

[3] U. Frisch, B. Hasslacher, and Y. Pomeau. Lattice-gas automata for the navier-stokes equation. *Phys. Rev. Lett.*, 56:1505–1508, Apr 1986.

[4] G. Krstulovic, M. Cencini, and J. Bec. Effective rates in dilute reaction-advection systems for the annihilation process $a + a \to \emptyset$. *Journal of Statistical Physics*, 153(3):530–550, Nov 2013.

[5] Lars Onsager. Crystal statistics. i. a two-dimensional model with an order-disorder transition. *Phys. Rev.*, 65:117–149, Feb 1944.

[6] C. N. Yang. The spontaneous magnetization of a two-dimensional ising model. *Phys. Rev.*, 85:808–816, Mar 1952.

[7] Gérard Y. Vichniac. Simulating physics with cellular automata. *Physica D: Nonlinear Phenomena*, 10(1):96–116, 1984.

[8] E. Goles and S. Rica. Irreversibility and spontaneous appearance of coherent behavior in reversible systems. *The European Physical Journal D*, 62(1):127–137, Mar 2011.

[9] Rodrigo Soto and Ramin Golestanian. Run-and-tumble dynamics in a crowded environment: Persistent exclusion process for swimmers. *Phys. Rev. E*, 89:012706, Jan 2014.

[10] John Cardy and Robert M. Ziff. Exact results for the universal area distribution of clusters in percolation, ising, and potts models. *Journal of Statistical Physics*, 110(1):1–33, Jan 2003.

[11] Tamotsu Kohyama. Cluster growth in particle-conserving cellular automata. *Journal of Statistical Physics*, 63(3):637–651, May 1991.

[12] Y Pomeau. Invariant in cellular automata. *Journal of Physics A: Mathematical and General*, 17(8):L415, jun 1984.

[13] H J Hermann, H O Carmesin, and D Stauffer. Periods and clusters in ising cellular automata. *Journal of Physics A: Mathematical and General*, 20(14):4939, oct 1987.

[14] C Moukarzel and N Parga. On the evaluation of magnetisation fluctuations with q2r cellular automata. *Journal of Physics A: Mathematical and General*, 22(8):943, apr 1989.

[15] Felipe Urbina and Sergio Rica. Master equation approach to reversible and conservative discrete systems. *Phys. Rev. E*, 94:062140, Dec 2016.

[16] Marco Montalva-Medel, Sergio Rica, and Felipe Urbina. Phase space classification of an ising cellular automaton: The q2r model. *Chaos, Solitons & Fractals*, 133:109618, 2020.

[17] Felipe Urbina. Equilibrium and nonequilibrium in the three-dimensional q2r cellular automata. *Phys. Rev. E*, 101:012111, Jan 2020.

[18] John Humphreys, Gregory S. Rohrer, and Anthony Rollett. Chapter 16 - computer modeling and simulation of annealing. In John Humphreys, Gregory S. Rohrer, and Anthony Rollett, editors, *Recrystallization and Related Annealing Phenomena (Third Edition)*. Elsevier, Oxford, third edition edition, 2017.

[19] Fran çois Graner and James A. Glazier. Simulation of biological cell sorting using a two-dimensional extended potts model. *Phys. Rev. Lett.*, 69:2013–2016, Sep 1992.

[20] G. Grimmett. *Percolation*. Die Grundlehren der mathematischen Wissenschaften in Einzeldarstellungen. Springer, 1999.

[21] Andrew Ilachinski. *Cellular Automata: A Discrete Universe*. World Scientific, Singapore, 2001.

[22] J. von Neumann. First draft of a report on the edvac. *IEEE Annals of the History of Computing*, 15(4):27–75, 1993.

[23] J. von Neumann. *Theory of Self-Reproducing Automata*. University of Illionois Press, Champain, IL, 1966.

[24] Raghu Raghavan. Cellular automata in pattern recognition. *Information Sciences*, 70(1):145–177, 1993.

[25] Tommaso Toffoli. Cam: A high-performance cellular-automaton machine. *Physica D: Nonlinear Phenomena*, 10(1):195–204, 1984.

[26] Stephen Wolfram. Statistical mechanics of cellular automata. *Rev. Mod. Phys.*, 55:601–644, Jul 1983.

[27] J Epstein and R Axtell. *Growing Artificial Societies: Social science from the bottom up*. MIT Press, Cambridge, USA, November 1996.

[28] Per Bak, Kan Chen, and Chao Tang. A forest-fire model and some thoughts on turbulence. *Physics Letters A*, 147(5):297–300, 1990.

[29] Andy Ilachinski. Irreducible semi-autonomous adaptive combat (isaac): An artificial-life approach to land combat. *Military Operations Research*, 5(3):29–46, 2000.

[30] S Wolfram. *Cellular Automata And Complexity: Collected Papers (1st ed.)*. CRC Press, Boca Raton, 1994.

[31] Stephen Wolfram. *A New Kind of Science*. Wolfram Media, 2002.

[32] Matthew Cook. Universality in elementary cellular automata. *Complex systems*, 15:1–40, Jan 2004.

[33] Alan M. Turing. On computable numbers, with an application to the Entscheidungsproblem. *Proceedings of the London Mathematical Society*, 2(42):230–265, 1936.

[34] Rodrigo Soto and Ramin Golestanian. Run-and-tumble dynamics in a crowded environment: Persistent exclusion process for swimmers. *Phys. Rev. E*, 89:012706, Jan 2014.

[35] Claudio Castellano, Santo Fortunato, and Vittorio Loreto. Statistical physics of social dynamics. *Rev. Mod. Phys.*, 81:591–646, May 2009.

[36] Mehran Kardar. *Statistical Physics of Particles*. Cambridge University Press, 2007.

[37] James Sethna. *Statistical Mechanics: Entropy, Order Parameters and Complexity (Oxford Master Series in Physics)*. Oxford University Press, 2006.

[38] J.M. Yeomans. *Statistical Mechanics of Phase Transitions*. Oxford Science, first edition, 1992.

[39] Praveen Chaddah. *First Order Phase Transitions of Magnetic Materials: Broad and Interrupted Transitions*. CRC Press, Boca Ratón, 1st edition, 2017.

[40] Sacha Friedli and Velenik Yvan. *Statistical Mechanics of Lattice Systems: a Concrete Mathematical Introduction*. Cambridge University Press, 2017.

[41] Ernst Ising. Beitrag zur theorie des ferromagnetismus. *Zeitschrift für Physik*, 31:253–258, 1925.

[42] Edward Fredkin and Tommaso Toffoli. Conservative Logic. *International Journal of Theoretical Physics*, 21(3-4):219–253, April 1982.

[43] Felipe Urbina. *Equilibrium and Non-Equilibrium in a Reversible and Conservative Cellular Automaton*. PhD thesis, Facultad de Ingeniería y Ciencias, Universidad Adolfo Ibañez, 2017.

[44] Renfrey B. Potts. Some generalized order-disorder transformations. *Mathematical Proceedings of the Cambridge Philosophical Society*, 48:106 – 109, 1952.

[45] F. Y. Wu. The potts model. *Rev. Mod. Phys.*, 54:235–268, Jan 1982.

[46] Massimo Ostilli and Farrukh Mukhamedov. 1d three-state mean-field potts model with first- and second-order phase transitions. *Physica A: Statistical Mechanics and its Applications*, 555:124415, 2020.

[47] Y Pomeau and G Y Vichniac. Extensions of q2r: Potts model and other lattices. *Journal of Physics A: Mathematical and General*, 21(15):3297, aug 1988.

Appendix A

Dynamics in $L = 256$, $L = 512$, $L = 1024$ and $L = 2048$

The following appendix shows the dynamics of the Q2R-Potts cellular automaton considering all the lengths explored during our study, in order to show its invariance to the size of the system. In addition, we show the dynamics of the configuration in the chain of length $L = 1024$ which presents the longest clusters during its evolution.

A.1 $L = 256$

Order

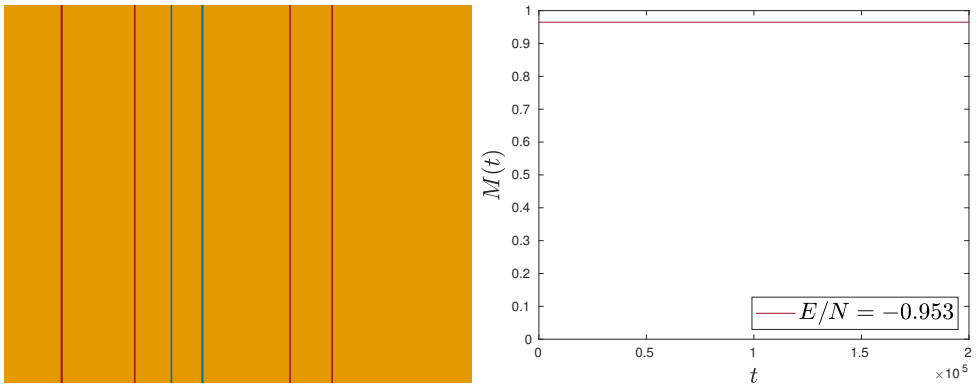

(a) (b)

Figure A.1: Temporal evolution (a) and magnetization (b) for the energy density $E/L = -0.953$ in a chain of length $L = 256$. Source: Own Elaboration.

Fluctuations

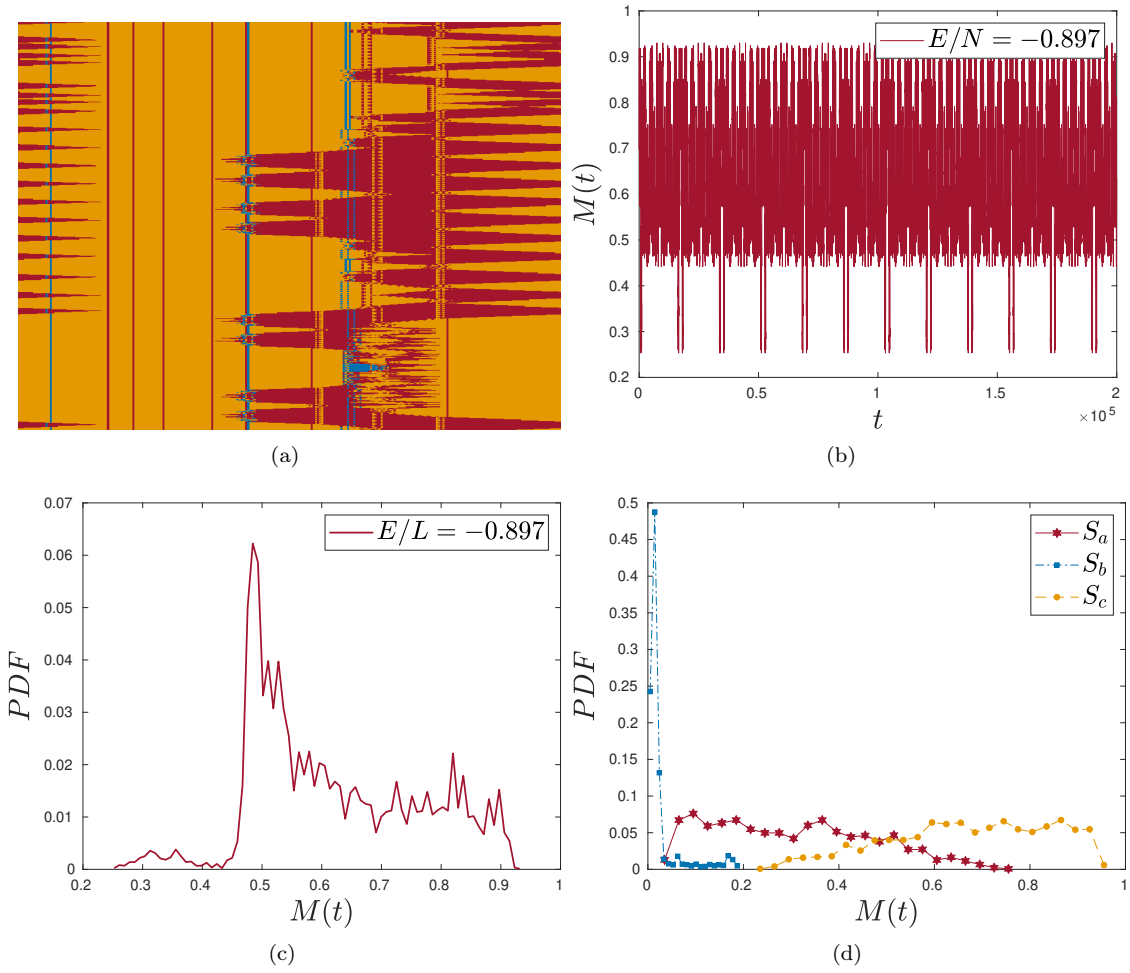

Figure A.2: Temporal evolution (a), magnetization (b), and probability density distributions (c) and (d), for the energy density $E/L = -0.897$ in a chain of length $L = 256$. Source: Own Elaboration.

Disorder

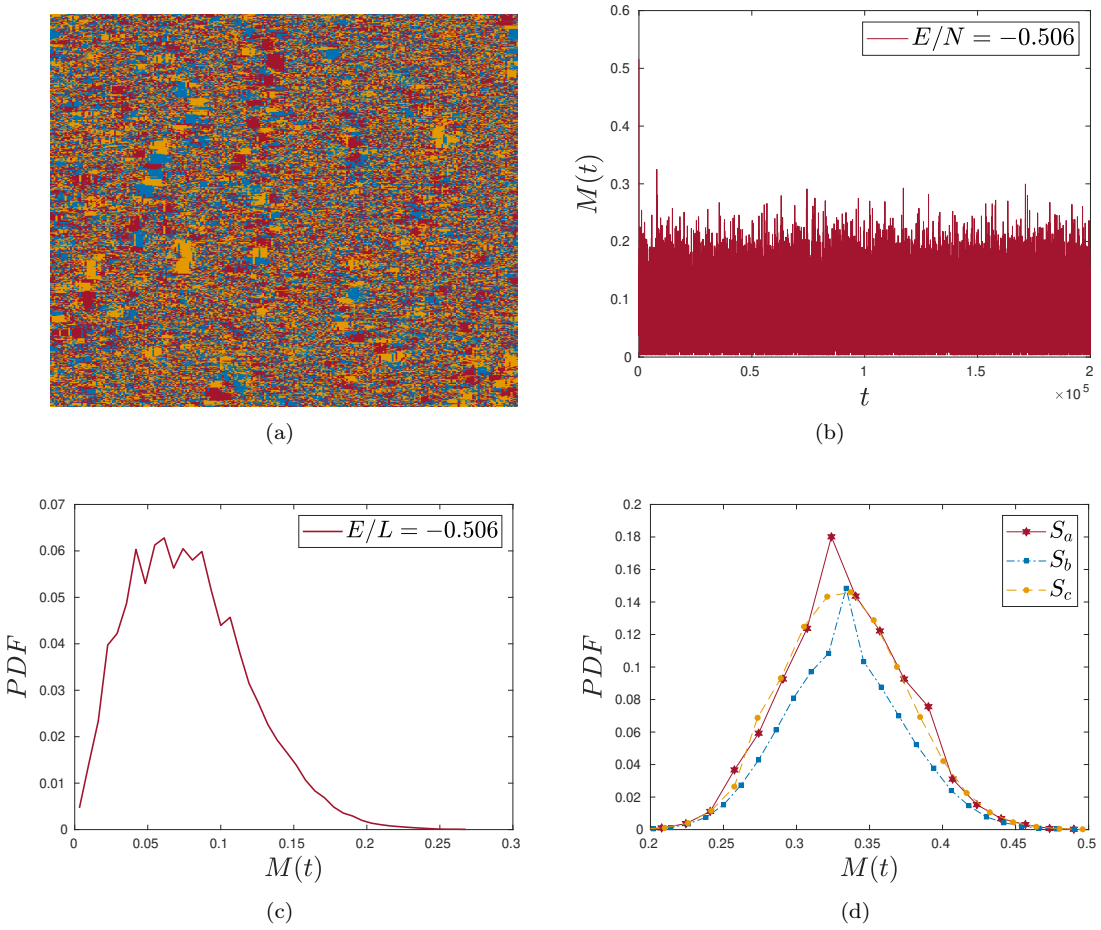

Figure A.3: Temporal evolution (a), magnetization (b), and probability density distributions (c) and (d), for the energy density $E/L = -0.506$ in a chain of length $L = 256$. Source: Own Elaboration.

A.2 $L = 512$

Order

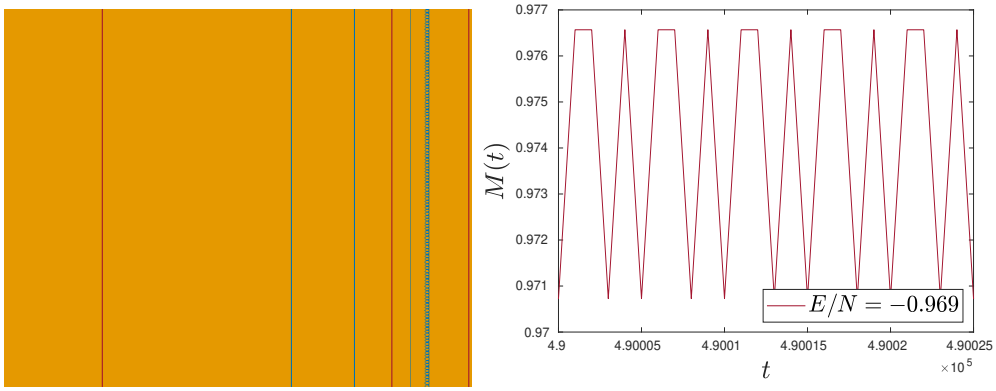

(a) (b)

Figure A.4: Temporal evolution (a) and magnetization (b) for the energy density $E/L = -0.969$ in a chain of length $L = 512$. Source: Own Elaboration.

Fluctuations

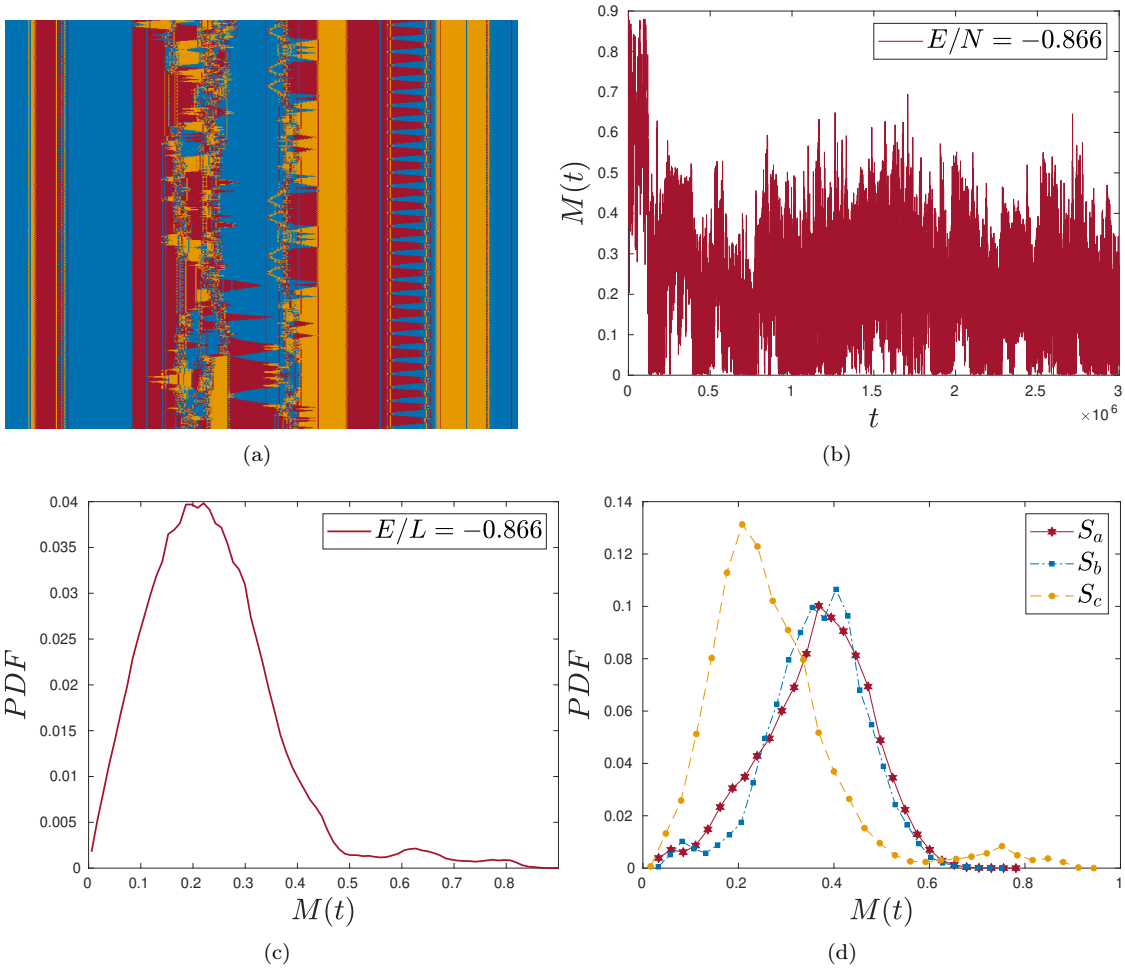

Figure A.5: Temporal evolution (a), magnetization (b), and probability density distributions (c) and (d), for the energy density $E/L = -0.866$ in a chain of length $L = 512$. Source: Own Elaboration.

Disorder

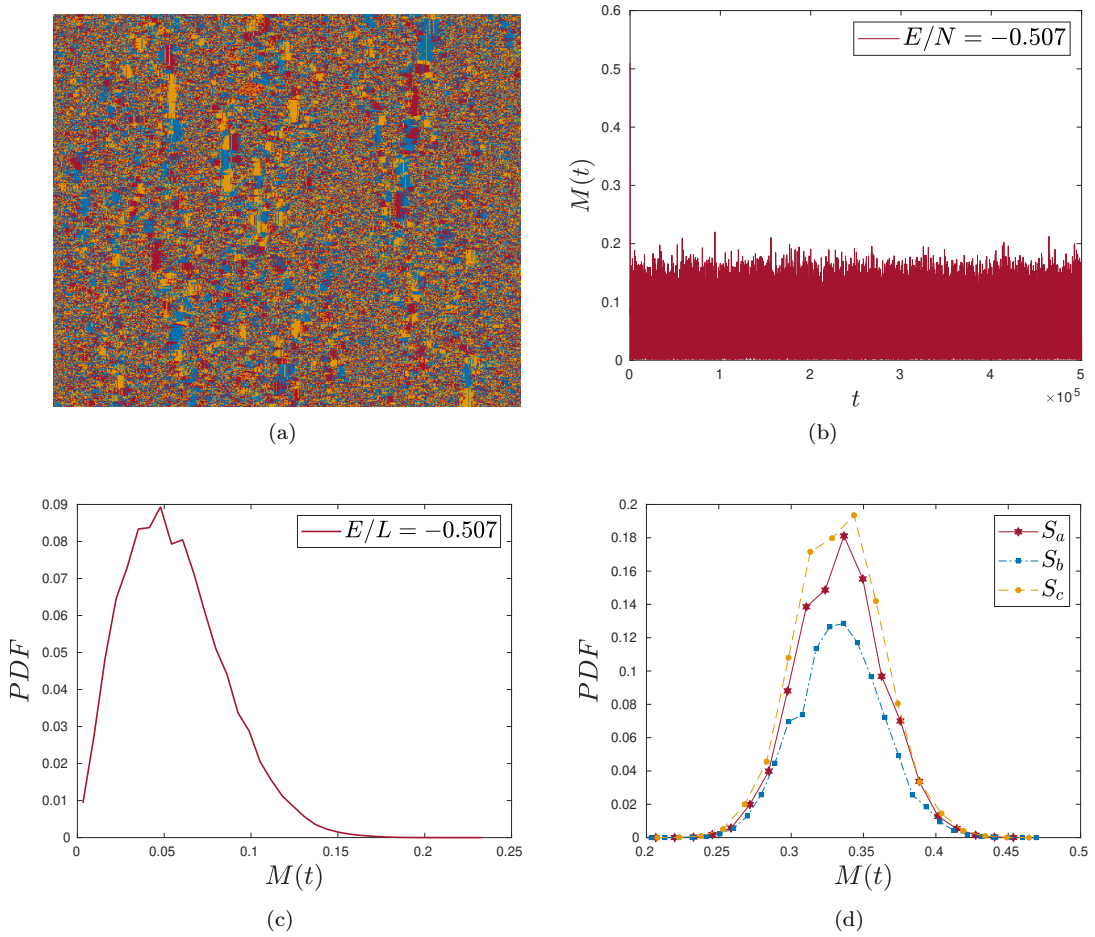

Figure A.6: Temporal evolution (a), magnetization (b), and probability density distributions (c) and (d), for the energy density $E/L = -0.507$ in a chain of length $L = 512$. Source: Own Elaboration.

A.3 $L = 1024$

Dynamic of the Configuration with the Largest Clusters

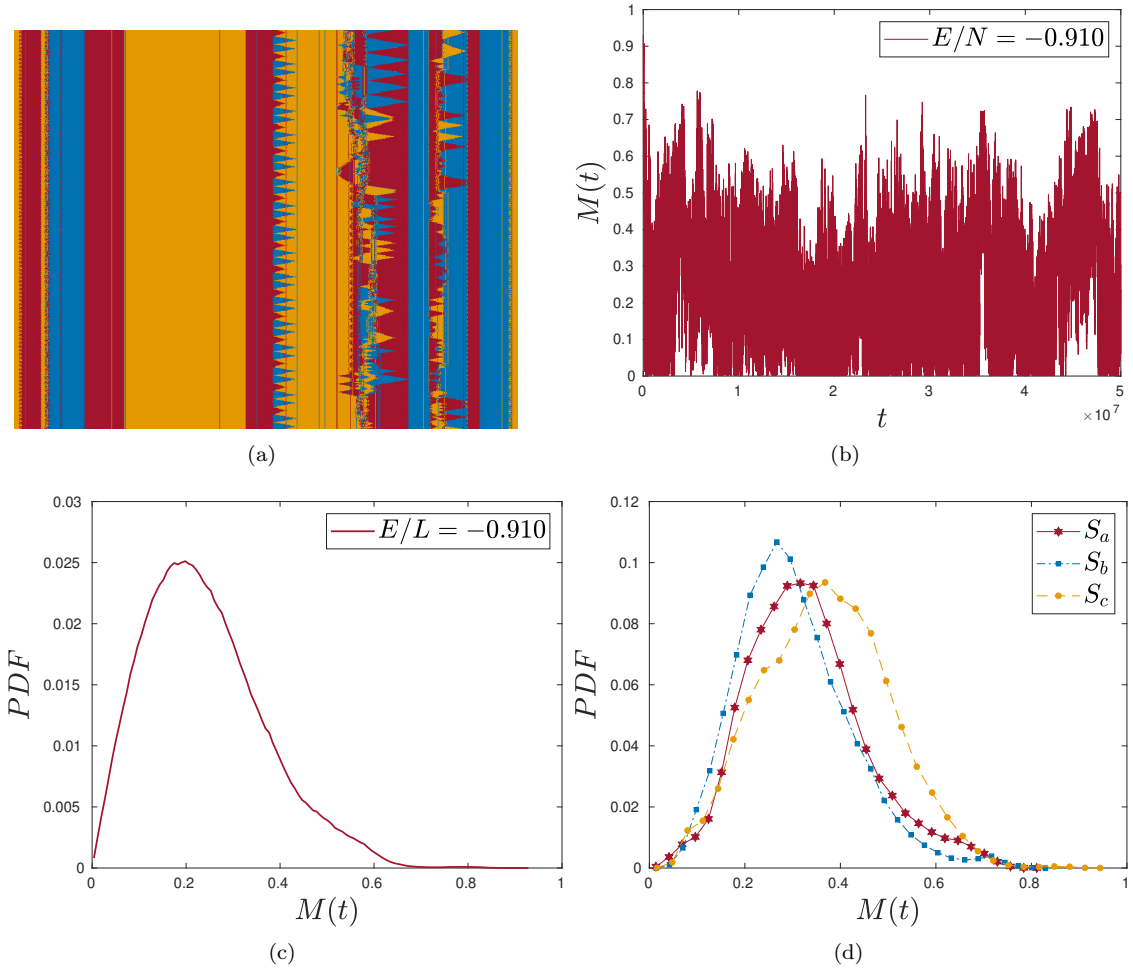

Figure A.7: Temporal evolution (a), magnetization (b), and probability density distributions (c) and (d), for the energy density $E/L = -0.910$ in a chain of length $L = 1024$. Source: Own Elaboration.

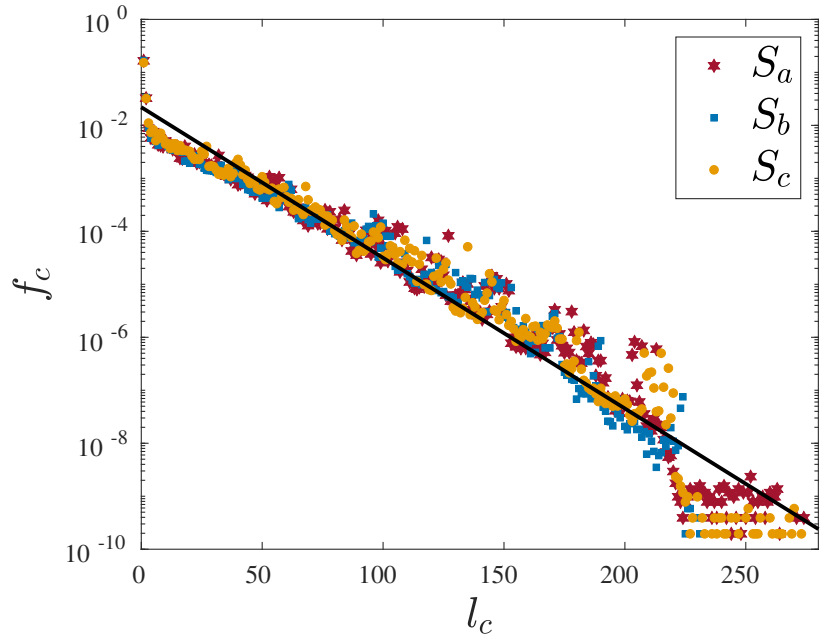

Figure A.8: Frequency of clusters versus its length for the energy density $E/L = -0.910$. Source: Own Elaboration.

A.4 $L = 2048$

Order

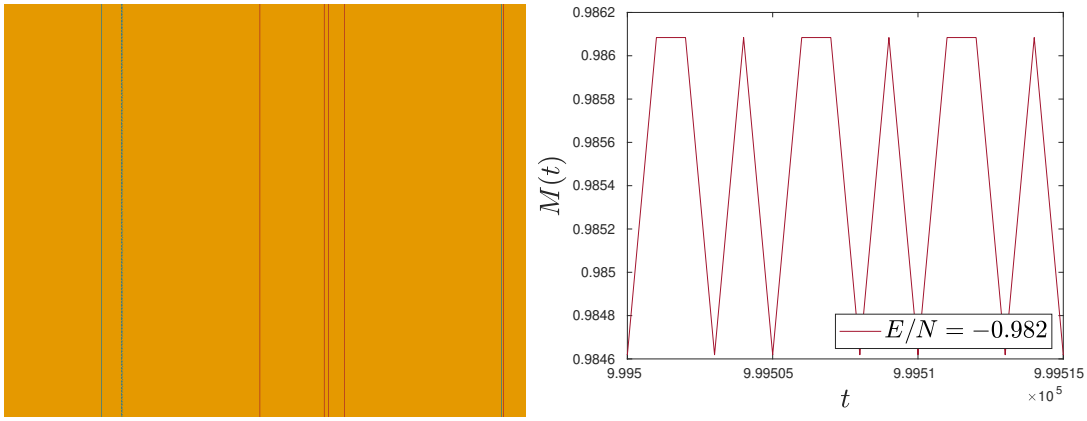

(a) (b)

Figure A.9: Temporal evolution (a) and magnetization (b) for the energy density $E/L = -0.982$ in a chain of length $L = 2048$. Source: Own Elaboration.

Fluctuations

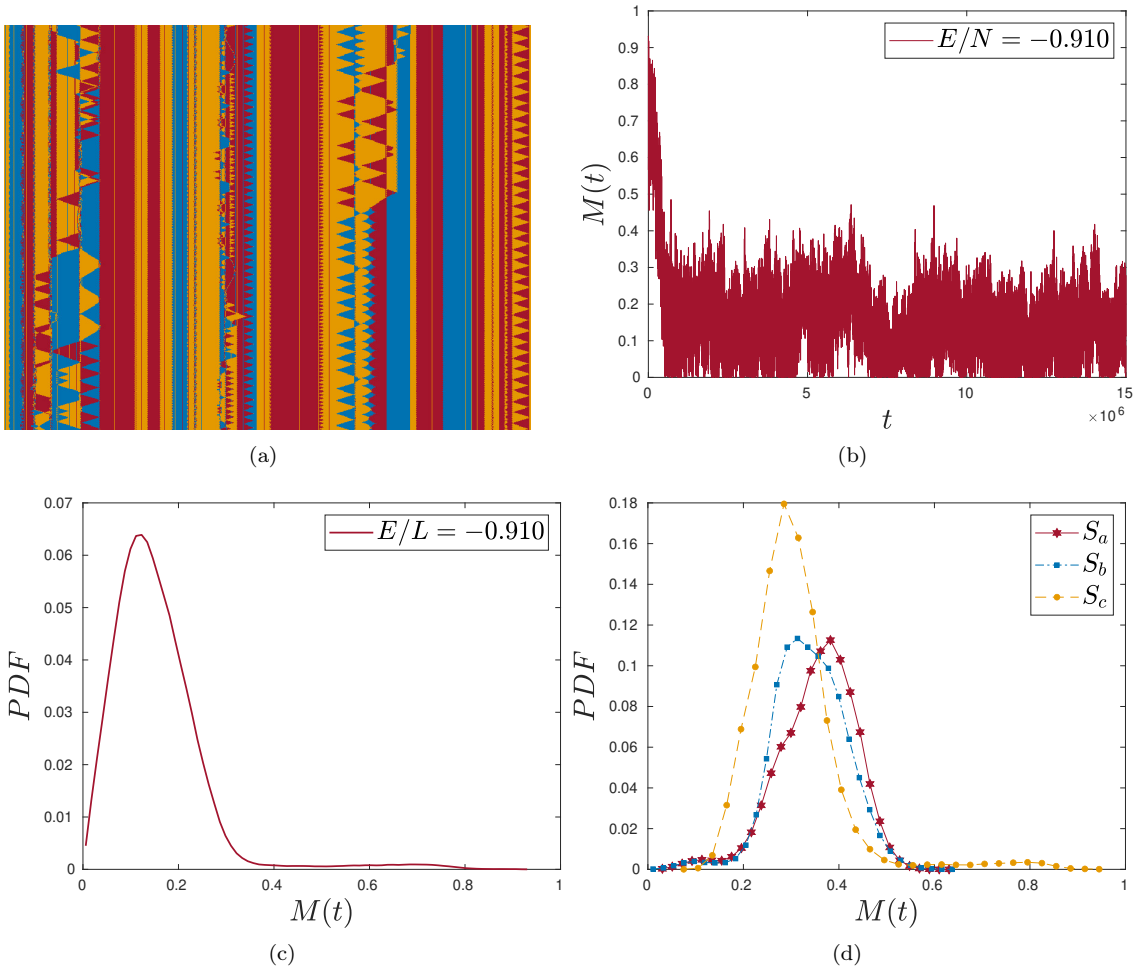

Figure A.10: Temporal evolution (a), magnetization (b), and probability density distributions (c) and (d), for the energy density $E/L = -0.910$ in a chain of length $L = 2048$. Source: Own Elaboration.

Disorder

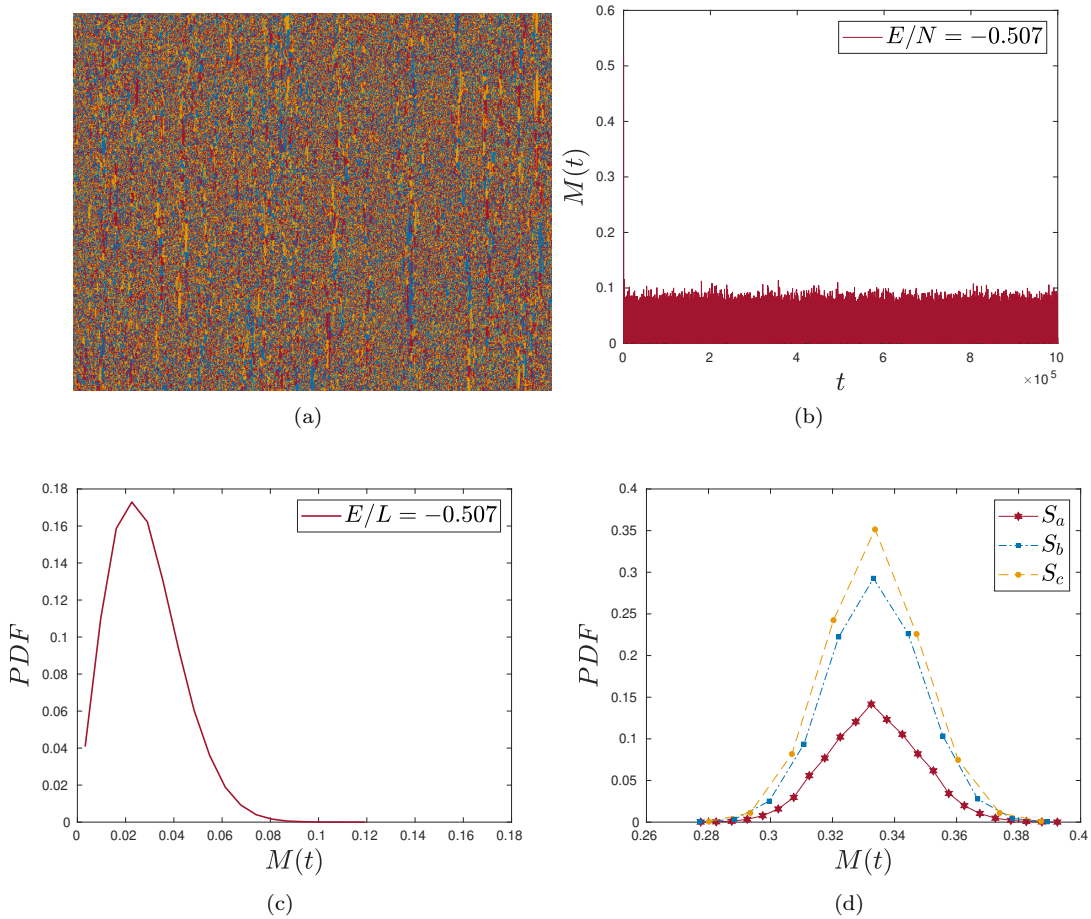

Figure A.11: Temporal evolution (a), magnetization (b), and probability density distributions (c) and (d), for the energy density $E/L = -0.507$ in a chain of length $L = 2048$. Source: Own Elaboration.